A toolbox for generating scalable mitral valve morphometric models

de Oliveira, Diana C.; Espino, Daniel M.; Deorsola, Luca; Mynard, Jonathan P.; Rajagopal, Vijay; Buchan, Keith; Dawson, Dana; Shepherd, Duncan E. T.

DOI:
10.1016/j.compbiomed.2021.104628

Document Version
Peer reviewed version

Citation for published version (Harvard):
de Oliveira, DC, Espino, DM, Deorsola, L, Mynard, JP, Rajagopal, V, Buchan, K, Dawson, D & Shepherd, DET 2021, 'A toolbox for generating scalable mitral valve morphometric models', *Computers in Biology and Medicine*, vol. 135, 104628. https://doi.org/10.1016/j.compbiomed.2021.104628

A toolbox for generating scalable mitral valve morphometric models

Diana C. de Oliveira[a,*], Daniel M. Espino[a], Luca Deorsola[b], Jonathan P. Mynard[c,d,e,f], Vijay Rajagopal[c], Keith Buchan[g], Dana Dawson[h,i], Duncan E.T. Shepherd[a]

[a] Department of Mechanical Engineering, University of Birmingham, Edgbaston, Birmingham, B15 2TT
* Corresponding author: DMC795@student.bham.ac.uk

[b] Paedriatic Cardiac Surgery, Ospedale Infantile Regina Margherita Sant Anna, Turin, 10126, Italy

[c] Department of Biomedical Engineering, The University of Melbourne, Melbourne, VIC 3010, Australia

[d] Heart Research, Murdoch Children's Research Institute, Royal Children's Hospital, Melbourne, VIC 3052, Australia

[e] Department of Paediatrics, The University of Melbourne, Melbourne, VIC 3010, Australia

[f] Department of Cardiology, Royal Children's Hospital, Melbourne, VIC 3052, Australia

[g] Department of Cardiothoracic Surgery, Aberdeen Royal Infirmary, Aberdeen, AB24 2ZN, Scotland

[h] School of Medicine, University of Aberdeen, Aberdeen, AB25 2ZD, Scotland

[i] Cardiology Department, Aberdeen Royal Infirmary, Aberdeen, AB25 2ZN, Scotland

Abstract

The mitral valve is a complex anatomical structure, whose shape is key to several traits of its function and disease, being crucial for the success of surgical repair and implantation of medical devices. The aim of this study was to develop a parametric, scalable, and clinically useful model of the mitral valve, enabling the biomechanical evaluation of mitral repair techniques through finite element simulations.

MATLAB was used to parameterize the valve: the annular boundary was sampled from a porcine mitral valve mesh model and landmark points and relevant boundaries were selected for the parameterization of leaflets using polynomial fitting. Several geometric parameters describing the annulus, leaflet shape and papillary muscle position were implemented and used to scale the model according to patient dimensions. The developed model, available as a toolbox, allows for the generation of a population of models using patient-specific dimensions obtained from medical imaging or averaged dimensions evaluated from empirical equations based on the Golden Proportion.

The average model developed using this framework accurately represents mitral valve shapes, associated with relative errors reaching less than 10% for annular and leaflet length dimensions, and less than 24% in comparison with clinical data. Moreover, model generation takes less than 5 minutes of computing time, and the toolbox can account for individual morphological variations and be employed to evaluate mitral valve biomechanics; following further development and validation, it will aid clinicians when choosing the best patient-specific clinical intervention and improve the design process of new medical devices.

Keywords: anatomy, biomechanics, computational, mitral valve, morphometry, parametric model

1. Introduction

The mitral valve (MV) is an anatomical structure, whose physiological function relies on the biomechanical properties and structural integrity of its components (Al-Atabi et al., 2012, Espino et al., 2007). Its shape is key to several traits of its function and disease, as shown by clinical (Lee et al., 2013, Sun et al., 2019), *in silico* (Pham et al., 2017, Caballero et al., 2020) and *in vitro* (Espino et al., 2007) studies. MV shape alterations, such as annular dilation or papillary muscle (PM) displacement, can affect MV performance, leading to regurgitation and resulting in suboptimal ventricular filling or ejection (Kohli et al., 2021, Cong et al., 2018).

Some common surgical interventions of the mitral valve include annuloplasty, leaflet resection, edge-to-edge repair or chordal replacement/transposition. Altering MV geometry during repair leads to changes in blood flow patterns, valve closure and ultimately disrupts normal flow through the left ventricle (LV) (Xu et al., 2021). Moreover, high/abnormal stresses which are induced on the valve leaflets post-repair may lead to post-surgical failure or impairment of valvular function (Kong et al., 2020). Therefore, the success of MV repair depends on the restoration of normal fluid dynamics, usually involving correction of valve mechanics (Al-Atabi et al., 2012). MV geometry has been exploited to improve the design of medical devices through the development of annuloplasty ring designs which 1) mimic the native annular saddle-shape (Doll et al., 2019) and 2) optimise load bearing by the annulus (Ncho et al., 2020), for example. The evaluation of pre- and post-operative scenarios which account for a subject's MV shape have the potential to improve surgical planning, specifically patient-specific repair procedures (Kohli et al., 2021, Walczak et al., 2021).

Computational studies have focused on diseased MV shapes (Caballero et al., 2019, Biffi et al., 2019, Aguilera et al., 2021) and surgical procedures (Choi et al., 2020, Caballero et al., 2020, Kong et al., 2018), either using structure-only finite element (FE) analysis (which allows to study leaflet stress patterns), or fluid-structure interaction (FSI) simulations (which accounts for the interaction between blood flow and the structure of the valve). The accuracy of these models is sensitive to valve geometry; however, even though several MV models from the literature are based on patient-specific geometries obtained from medical imaging, the associated generation process can be time consuming and computationally expensive, especially when employing numerical mesh-based approaches (Zhang et al., 2019). Moreover, deductions made from a patient-specific case cannot be generalized, since multiple patient-specific models are required for statistical power (Biau et al., 2008).

To overcome these limitations, parametric models, whose geometrical features are described by constraints such as specific dimensions/measurements, can be used. Some parametric MV models lack the anatomical detail that is necessary to be of clinical value, including only a simplistic representation of the leaflets (Salgo et al., 2002, Shen et al., 2017, Domenichini and Pedrizzetti, 2015). Other studies have included more complete parametric geometries including chordae tendineae and PM tips (Choi et al., 2016, Alleau et al., 2019), while more advanced parameterization frameworks have been recently developed to generate patient-specific MV surface models from measurements obtained via medical imaging (Lichtenberg et al., 2020, Pasta et al., 2020). While these advanced frameworks can generate high quality MV models within a reasonable time frame, they can only be applied to each specific patient individually, not offering the flexibility required to allow for the evaluation of how specific dimensions of MV geometry affects its function, for example.

Multiple *in vivo* (Warraich et al., 2012, Deorsola and Bellone, 2018, Oliveira et al., 2020) and *ex vivo* (Duplessis and Marchand, 1964, Okamoto et al., 2007) morphometric studies have attempted to correlate different dimensions of the MV geometry. Nonetheless, a unifying mathematical model that can be employed to generate an average MV geometry has been lacking in the literature. Given the importance of MV shape on the long-term outcome of valvular surgical procedures, there is a need to develop a computational framework which allows to generate scalable and customisable MV geometries, either 1) based on average morphometric relationships or 2) from patient-specific dimensions. A full description of the anatomy of the mitral valve has recently been made available, providing further insight into the complexity of mitral valve shape and how such information needs to be accounted for when developing geometrical models (Oliveira et al., 2020). A framework which could capture the range of morphological features required to address the high variability seen in clinical cases is not currently available and would aid in the clinical decision-making process. For example, such framework could be used to virtually evaluate mitral interventions in the case of unhealthy MV shapes by creating aimed post-repair configurations and assessing their associated biomechanics to determine the best indicators of performance.

The aim of this study was to develop a tool (entitled the MV toolbox) that enables the quick generation of anatomically accurate and clinically useful parametric models of the MV, which are compatible with biomechanical evaluation of mitral repair techniques through FE simulations. In this manuscript, a description of the MV toolbox is provided, including the development of the geometrical model, the equations implemented to evaluate the anatomical

dimensions, and the framework that generates a model ready to be used in computational modelling software.

2. Mitral valve toolbox

2.1 Generic features

A software toolbox that can generate the geometry of the MV as a computational model was developed and implemented in MATLAB (MATLAB®, R2019b, 9.7.0.1247435, The MathWorks Inc., Natick, MA, USA). The toolbox yields a diastolic (stress-free) MV geometry including the annulus, anterior and posterior leaflets, and a spatial representation for both PM. The model is built from a baseline mitral annular 3D profile adapted from literature (Pouch et al., 2014) and a set of key MV dimensions, used as constraints to generate the annulus and leaflet shapes. Then, PM spatial position is generated based on distances to key annular landmarks and chordae tendineae are created assuming equal spacing along the MV free edge and generated based on PM and selected free edge node coordinates.

The workflow of the toolbox is shown in Figure 1. The main geometric features of the MV annular and leaflet shape employed to generate the model follow mathematical proportions from recent literature (Deorsola and Bellone, 2018, Deorsola and Bellone, 2019), and PM positions and chordae tendineae distributions are based on *in vivo* and *ex vivo* findings (Yamaura, 2008, Obase et al., 2016, Lam et al., 1970). The model can be parameterized using two alternative procedures: (1) based on patient-specific dimensions obtained from patient data (e.g. medical image modalities) and directly inputted by the user or (2) using average dimensions derived from mathematical proportions relating MV anatomical segments based only on the anteroposterior (AP) diameter (Section 3).

Multiple graphic user interface (GUI) options are provided to better characterize the subvalvular apparatus: the user can choose a one tip point representation for the PM, where all chordae originate from, or a 3D origin scheme; moreover, PM displacement can be prescribed. Greater detail on all GUI options is provided in Section 2. The toolbox generates two different outputs: a MV geometrical model or a MV model for computational simulations (further detail on these options is presented below): Once the parameterization is completed, the MV leaflet surface mesh can be exported as a stereolithography (.stl) file, compatible with a range of modelling software (including computer-aided design and FE analysis software), and the 3D coordinates of the PM can be exported as a text file. On the other hand, if one chooses to create an input file for computational simulations, the chordae tendineae

distributions are also added, completing the MV model. The input file for FE simulations is compatible with LS-DYNA 4.5.12 (LSTC, Livermore CA, USA) and employs the generated geometry. For this, the meshed model is pre-processed by defining material properties, boundary conditions and contact properties through MATLAB, with the LS-DYNA input file being exported as a key (.k) file.

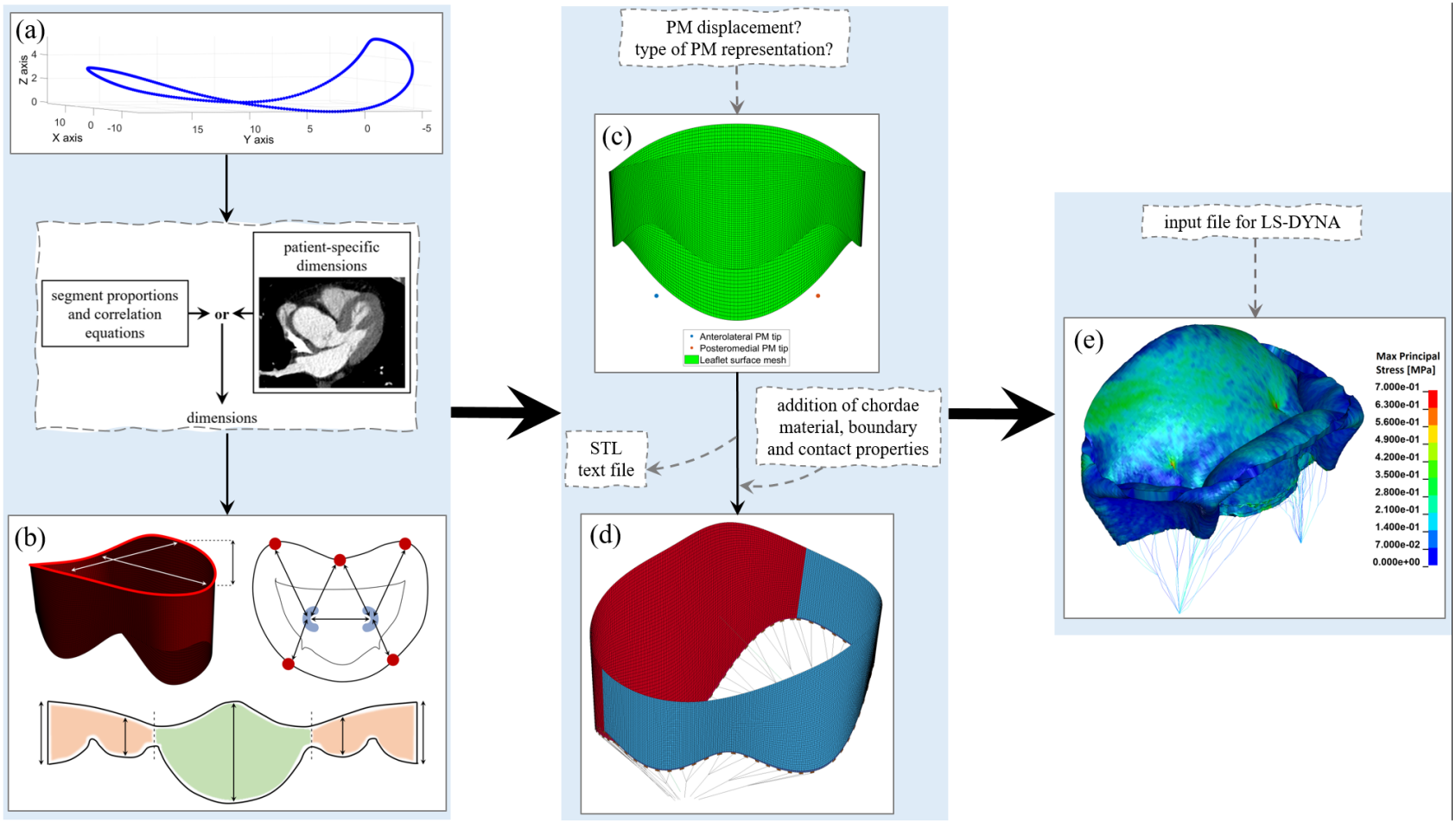

Figure 1. Workflow of the MV toolbox, from the generation of the morphometric model to the FE simulation result: (a) The inputs are a baseline mitral annular 3D profile and MV dimensions, either obtained from mathematical formulations or from patient-specific medical images; (b) The model is parameterized, with the annulus, leaflets and PM (papillary muscles) being independently scaled; (c) A surface model mesh is created for the leaflets and points identifying each PM are stored. The user can choose to output these as an .stl file for the mesh and a text file for PM coordinates; (d) The meshed model is pre-processed: chordae tendineae are added, material properties, boundary and contact conditions are defined; (e) The .k input file is created and run in LS-DYNA.

2.2 Geometrical model

2.2.1 Pre-processing and assumptions

MATLAB was used to define the annular saddle (Figure 2) based on a mean annular height to commissural width ratio (AHCWR) rotational profile for a healthy adult obtained from Pouch *et al.* (2014) which was adapted to define annular height (over the *z*-coordinate, displayed in Figure 2) (Pouch et al., 2014). Moreover, data from Jassar *et al.* (2014) was employed to change the annulus in the *x*-*y* plane (Figure 2) (Jassar et al., 2014). The annulus was further reshaped to match a diastolic profile, obtaining an approximately 7.6 mm saddle-horn height, consistently with previous experimental findings (Dagum et al., 2001). This annular boundary was used as a starting template from which to recreate the MV geometry (Figure 1a). The model incorporates the following assumptions, according to the GUI options chosen by the user:

1. The annular and leaflet shapes are assumed symmetric along the long axis meridian of the anterior MV leaflet, consistent with *ex vivo* findings (Ranganathan et al., 1970, Krawczyk-Ozog et al., 2017) and previous geometrical models (Choi et al., 2016, Stevanella et al., 2009). The PM tips are assumed symmetric; however, this symmetry can be removed if asymmetric PM displacement is prescribed;
2. If an average model is selected, a healthy MV leaflet shape is reproduced, since, in disease, the proportions characterizing annular and leaflet segments change (Deorsola and Bellone, 2019). However, if patient-specific data is inputted, the model shape is not constrained when generated, and it is possible to create either a healthy or diseased MV model according to the input.

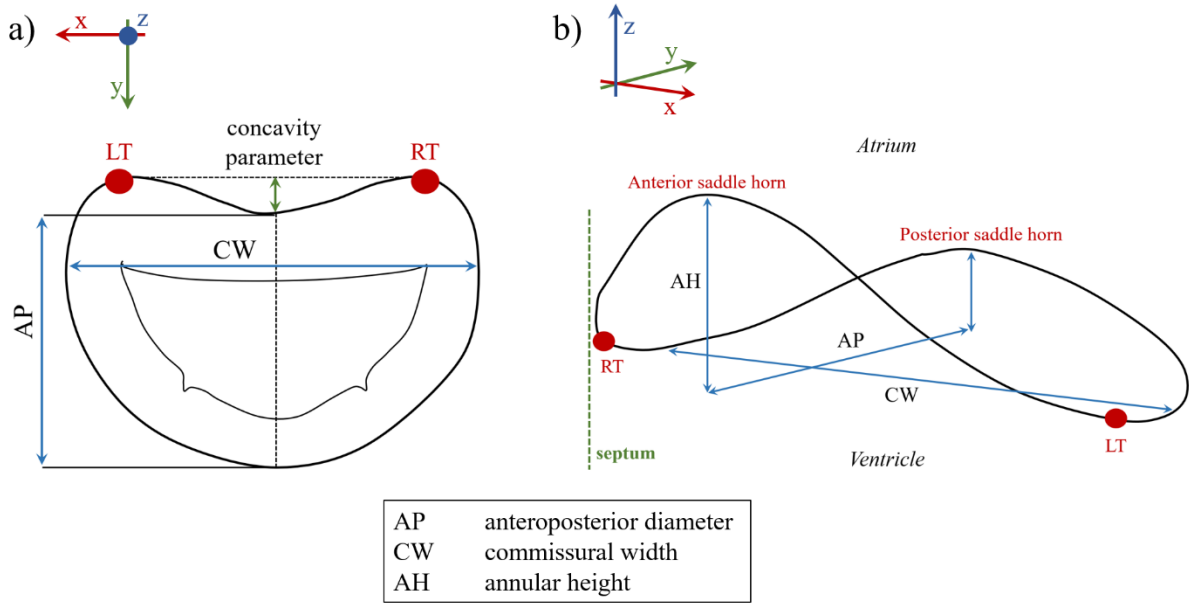

Figure 2. Input parameters requested in the toolbox to parameterize the annular boundary, where the MV annulus is a) viewed from within the left atrium and b) from above. The 3D axis denote the orientation for each image. Notes: LT, left trigone; RT, right trigone.

The generation of a morphometric MV model focuses on 3 regions: first the annulus is parameterized, followed by the anterior and posterior leaflets, and lastly the PM tips.

2.2.2 Annular parameterization

All dimensions needed to parameterize the mitral annulus are included in Figure 2. The valve ring has a kidney bean shape, more evident in systole, and the anterior leaflet is centred on a slight depression in this ring (Degandt et al., 2007, Misfeld and Sievers, 2007). Accounting for a previous mathematical study of the MV (Kaiser et al., 2019), the valve ring concavity can be controlled given an input parameter that varies between 0 and 0.5: 0 corresponds to a D-shaped annulus, while 0.5 represents the maximum allowed concavity.

After defining the ring concavity, the annulus can be parameterized using three dimensions: the AP diameter, the commissural width (CW) and the annular height (AH). The best fitting polynomial curves were selected to manipulate the annular shape: first, they were used to scale the AP diameter and CW in the *x*-*y* plane; then, the AH was parameterized using polynomial curves to scale *z* coordinates. AH was defined as the vertical distance between the maximum and minimum annular heights (Jassar et al., 2014, Pouch et al., 2014), and, by default, characterised as the anterior saddle horn height. By scaling this height, the posterior

saddle horn height was appropriately scaled, maintaining the proportion between anterior and posterior saddle horn heights.

2.2.3 Leaflet parameterization

Given the assumed symmetry of the MV, the heights of the anterolateral and posteromedial commissural scallops were considered equal. The required MV dimensions to parameterize the leaflets are shown in Figure 3. The initial 3D free edge template was generated according to the inputted leaflet heights and baseline commissural heights (to be adapted during the implementation) reported by Ranganathan et al (Ranganathan et al., 1970), which were interpolated.

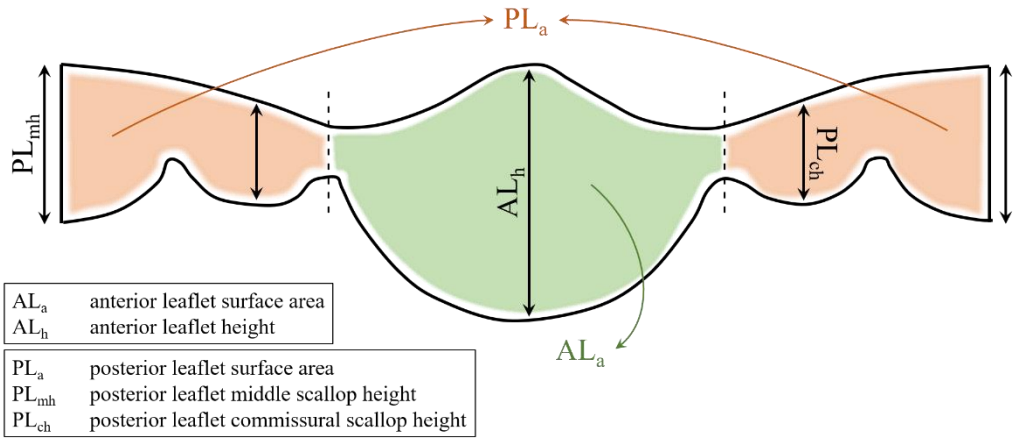

Figure 3. Input parameters requested in the toolbox to parameterize the leaflets.

To parameterize the leaflet surface areas, both annular and free edge boundaries were split into different portions representing the anterior leaflet and the posterior middle and commissural scallops. For this process, the annular boundary was first split considering anterior and posterior annular proportions (2/5 and 3/5 of the total annular circumference, respectively (Pouch et al., 2014, Jassar et al., 2014)). The annular split point has been set as the commissural point. In addition, the posterior leaflet middle scallop is usually broader than the other two scallops (Ranganathan et al., 1970, Krawczyk-Ozog et al., 2017); therefore, to divide the posterior leaflet annular boundary between middle and commissural scallops and in agreement with a previous morphometry study (Deorsola and Bellone, 2019), the middle scallop was assumed equal to 9/20 of the total posterior leaflet circumference. In the implementation, the length of the commissural and cleft boundaries was then altered to obtain

the desired leaflet areas. A representation of all leaflet boundaries employed is presented in Figure 4.

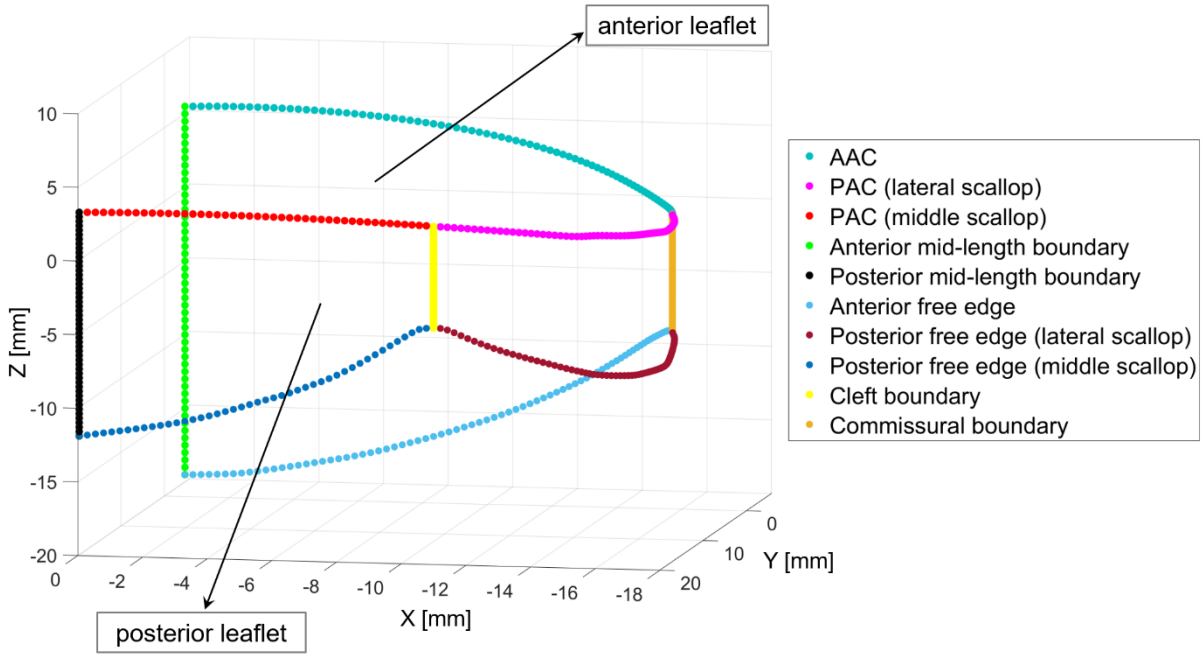

Figure 4. The lateral half of the MV is represented, with boundaries defined during the parameterization process of the leaflets. Notes: AAC, anterior annular circumference; PAC, posterior annular circumference.

2.2.4 Papillary muscle parameterization

The 3D spatial position of PM tips is parameterized according to distances between the tips and annular landmarks (o'clock points) (Yamaura, 2008, Sakai et al., 1999). Figure 5a represents these annular points and the implemented distances (within literature ranges). The user can decide whether to represent the PM as a single tip (where all chordae originate from), or as a 3D point cloud of chordae origins in a C-shape (as given in an axial view), discretized in Figure 5b and 5c and based on *in vivo* and *ex vivo* findings (Obase et al., 2016, Lam et al., 1970) and previous computational studies (Stevanella et al., 2011, Choi et al., 2016). This point cloud consists of 13 origin points per PM, giving rise to 12 anterior leaflet free edge insertions, 12 posterior leaflet free edge insertions and 2 strut chordae insertions. In total, it equals 26 chordae, consistent with *in vivo* (Obase et al., 2016) and *ex vivo* (Lam et al., 1970) findings.

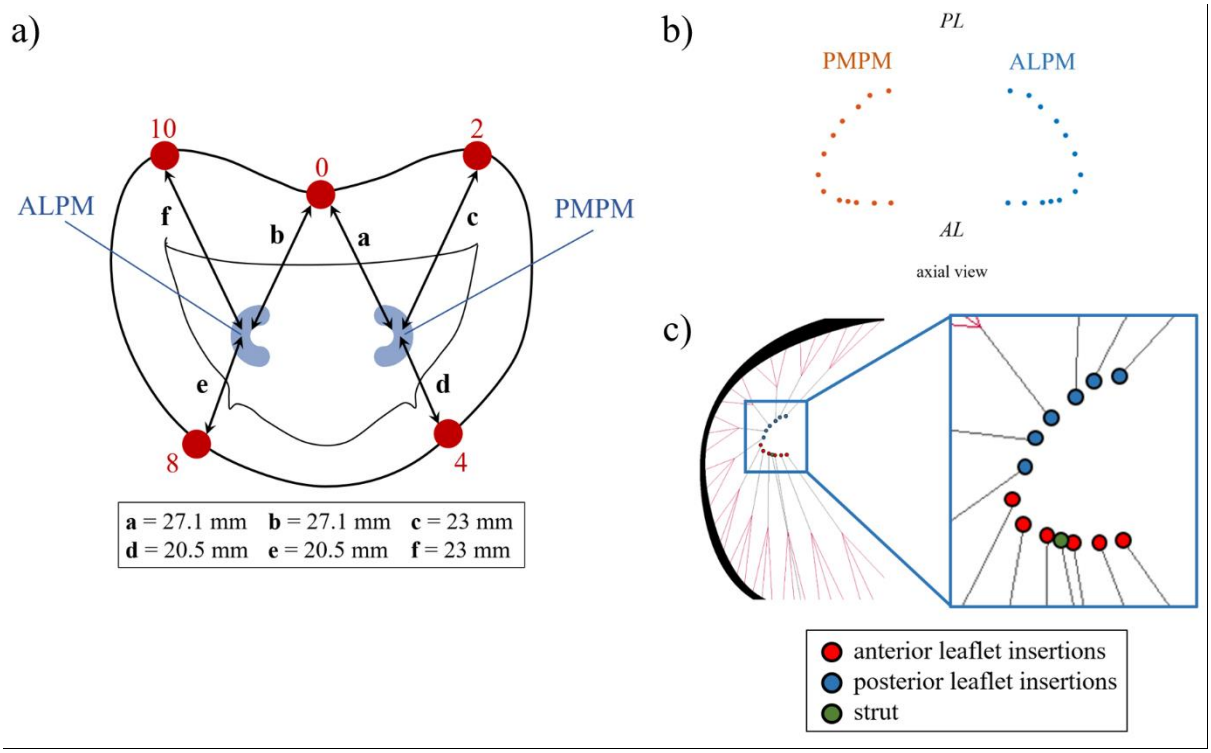

Figure 5. a) Distances between PM tips and corresponding points of mitral annulus, as characterized by the literature (Sakai et al., 1999, Yamaura, 2008). 0, 2, 10, 4 and 8 o'clock represent: anterior annular midpoint; right trigone; left trigone; division between middle and posteromedial commissural scallops; division between middle and anterolateral commissural scallops, respectively (Yamaura, 2008); b) 3D shape representing chordae origins in the PMs (axial view); c) Different origin points correspond to different points of insertion into the leaflets. Notes: ALPM, anterolateral PM; PMPM, posteromedial PM; PL, posterior leaflet; AL, anterior leaflet.

The spatial position of PM tips can be further manipulated to represent different dysfunctional situations (Figure 6). The PMs can undergo medial/lateral (position change in *x-y* plane) and apical (change in the *z*-coordinate) shifts, corresponding to malposition or change in position (Kim et al., 2012). These relate to symmetric (same motion restriction for both leaflets) or asymmetric (prevalent restriction of one of the leaflets) tethering, represented by displacement of both PMs or either one of them (Kim et al., 2012). Since these changes are associated with altered inter-PM distances (Kim et al., 2014, Obase et al., 2016), the user needs to provide the desired inter-PM distance as an input.

As the LV dilates, the PM also get displaced (Obase et al., 2016). In the toolbox, the user can prescribe whether the LV dilates posteriorly, anteriorly, or on both sides. An .stl file of a 18 year old (female, weight 68 kg, BSA 1.66 m^2) adolescent LV model was reconstructed from a magnetic resonance imaging (MRI) scan sequence obtained at the Murdoch Children's Research Institute (study approved by the Human Research Ethics Committee of the Royal Children's Hospital – HREC 33227): the left ventricle was scanned with a cine TrueFISP short axis stack sequence, using multiple breath-hold blocks, on a

Siemens Aera MRI at 1.5T (repetition time = 39.6 ms; echo time = 1.43; flip angle = 80 degrees; pixel spacing 1.33 × 1.33 mm; slice thickness = 7 mm; 25 frames over the cardiac cycle).

The reconstructed model was used as a template to approximate the inner geometry of the LV on which papillary muscles are placed. The model has been scaled to match adult dimensions from the literature (Di Donato et al., 2006) and arranged in the 3D space to align its base with the MV annular plane, similar to previous computational studies (Park et al., 2019, Domenichini and Pedrizzetti, 2015, Domenichini et al., 2005). The geometry can be then parameterized based on the input width and length (Park et al., 2019, Di Donato et al., 2006, Domenichini and Pedrizzetti, 2015). The distance between the tip of each PM and its respective site of origin at the LV wall was assumed 26 mm, yielding a PM base within the middle third of the wall (Saha and Roy, 2018). By parameterizing the LV geometry, the position of the PM base is also rearranged, and, if the respective distance between tip and base is greater than 8.8 mm (standard deviation for this distance (Saha and Roy, 2018)), the tip is displaced (as displayed in the schematic from Figure 7).

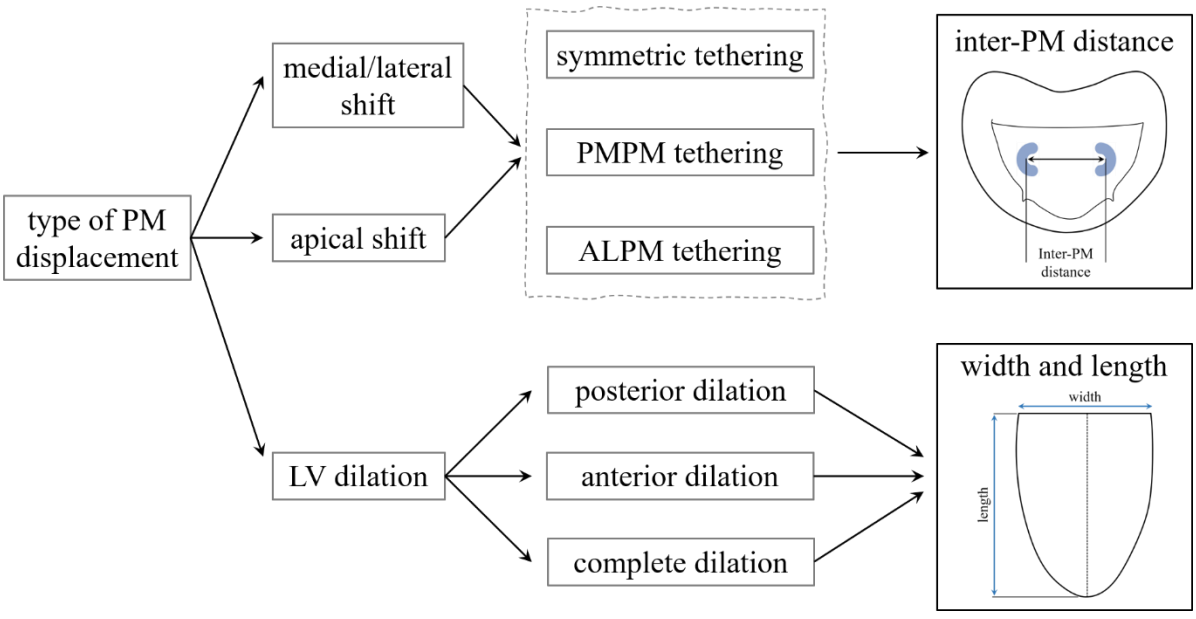

Figure 6. GUI options for the definition of PM displacement in a dysfunctional case. Notes: PM, papillary muscle; ALPM, anterolateral papillary muscle; PMPM, posteromedial papillary muscle; LV, left ventricle.

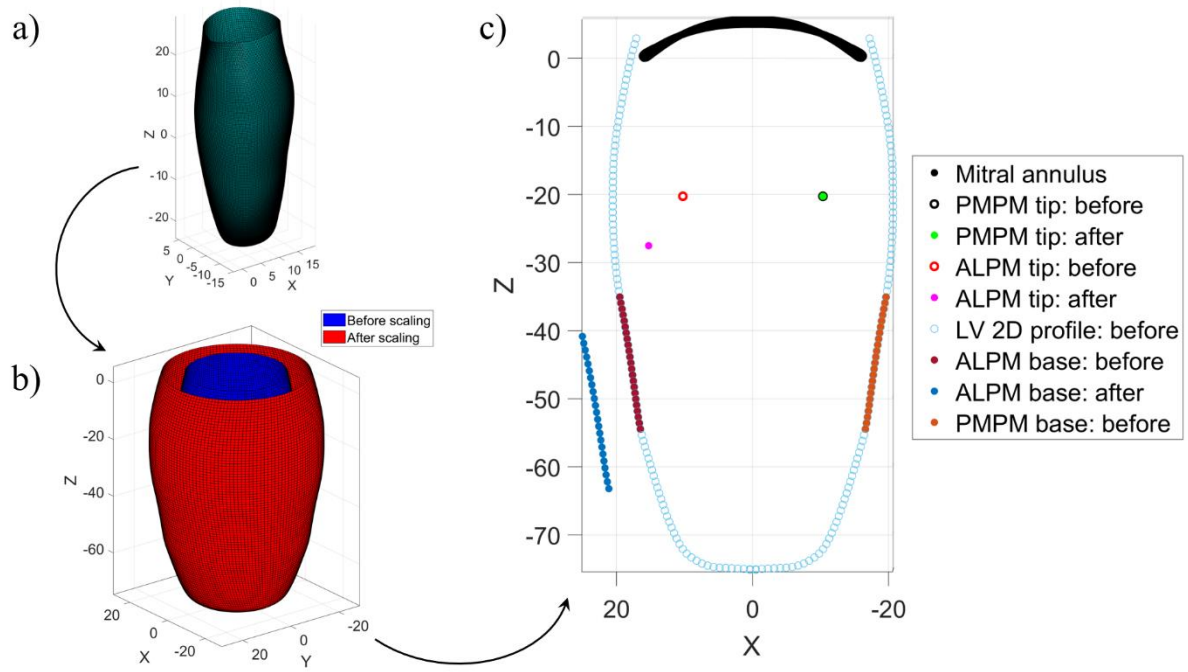

Figure 7. MATLAB process of PM displacement due to LV dilation: a) A LV 3D model reconstructed from MRI imaging is employed as a template, which can be scaled according to input dimensions for width and length (b)); c) A 2D cross-section representation of PM displacement due to LV dilation is displayed, including positions for PMPM and ALPM before and after LV scaling. In a scenario where LV anterior dilation occurs, the position of the anterior PM base is altered accordingly, leading to ALPM displacement. Notes: PM, papillary muscle; ALPM, anterolateral papillary muscle; PMPM, posteromedial papillary muscle; LV, left ventricle.

2.2.5 Chordae generation

All but the strut chordae are assumed to attach at the free edge (primary chordae) and secondary chordae are not included in the toolbox. Primary chordae are equally spaced along the free margin and, based on the generated leaflet geometry, insertion points in the free edge are created according to the number of chordae branches to include: they split into three branches in the case of a single PM point and if the PM is represented with a 3D shape. Chordae are branched at a node midway between the PM origin node and the free margin: finding this node involves obtaining the midway point between three free margin nodes and then the midway point between that point and the PM origin node. Examples of virtually created chordae tendineae with a single PM tip and a 3D PM shape are shown in Figure 8.

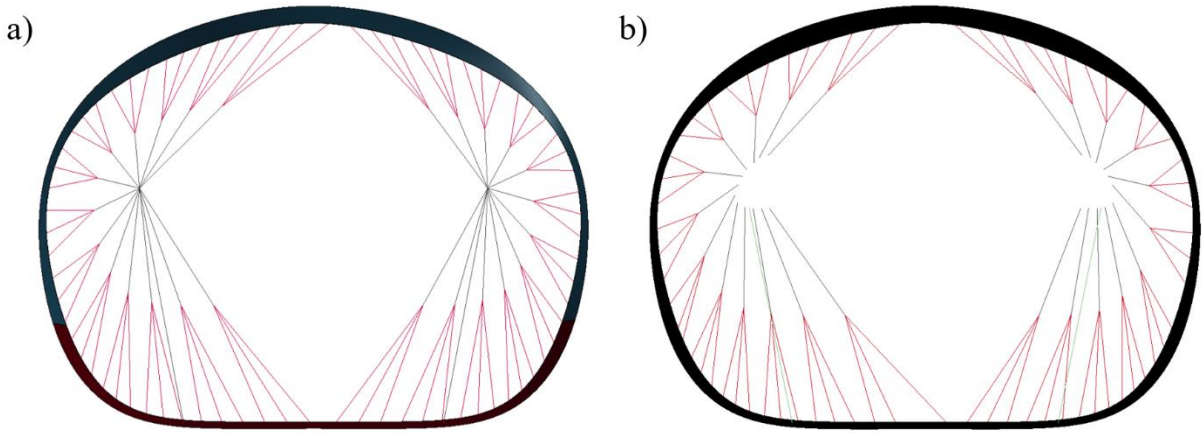

Figure 8. a) Single PM tip (left) and b) 3D PM shape (right) chordae tendineae distributions.

3. Morphometric evaluation: The Golden Proportion

3.1 Equations employed for average model

Recently, two clinical studies have shed light on the use of the Golden Proportion to define the geometrical structure of the healthy MV (Deorsola and Bellone, 2018, Deorsola and Bellone, 2019). This proportion has been observed in nature (Iosa et al., 2013, Ferring and Pancherz, 2008, Henein et al., 2011) and consists of a ratio obtained from sectioning a certain segment in two different parts (Deorsola and Bellone, 2018). The use of the Golden Proportion to characterize MV geometry has been assessed by previous studies (Deorsola and Bellone, 2018, Deorsola and Bellone, 2019) and the corresponding formulae are employed in the MV toolbox to generate the annular and leaflet parts from one single input dimension: the AP diameter. Further detail on this ratio can be found elsewhere (Deorsola and Bellone, 2019). The equations that define the annulus are:

$$d_{CW} = 1.236 d_{AP}, \quad (1)$$

$$h_{AH} = 0.236 d_{AP}, \quad (2)$$

where d_{CW} is the commissural width, h_{AH} is the annular height and d_{AP} is the anteroposterior diameter. Assuming the annular boundary as a circumference, the annular radius is equal to half of the CW. As for leaflet heights, the anterior leaflet height is defined equal to the AP diameter and the posterior leaflet heights are defined as below:

$$P_{mh} = r = 0.618 d_{AP}, \quad (3)$$

$$P_{ch} = 0.618^2 d_{AP}, \quad (4)$$

where r is the annular radius, P_{mh} and P_{ch} are the posterior leaflet middle and commissural scallop heights, respectively. The leaflets are mathematically defined as half-ellipses:

$$A_a = \pi \frac{[4.236 r^2]}{4} = 0.4045 \pi {d_{AP}}^2 \quad (5)$$

$$P_a = \pi \frac{[2.854 r^2]}{4} = 0.2725 \pi {d_{AP}}^2 \quad (6)$$

where A_a and P_a are the anterior and posterior leaflet surface areas, respectively.

3.2 Validation

3.2.1 Annular parameters

Given the dynamic variability in annular shape during the cardiac cycle (Jiang et al., 2014) and the fact that the Golden Proportion equations better represent a diastolic MV configuration (Deorsola and Bellone, 2018), mid-diastolic data was employed for validation of the Golden Proportion predictions. For this, mid-systolic data was retrieved from adult and paediatric *in vivo* studies and converted to mid-diastolic values: variations of -9% and +3% were employed for AH and CW data, respectively, based on clinical findings (Tang et al., 2019, Levack et al., 2012, Maffessanti et al., 2013). For end-systolic data, the same values were used. Predictions for CW and AH, as provided by clinical data and derived from the Golden Proportion, are present in Figure 9 a) and b), while goodness-of-fit is explored in Figure 9 c) and d). The Golden Proportion equations appear able to predict CW and AH values from the AP diameter, as given by R-squared values of 0.83 and 0.91, respectively. The average relative errors between predicted average values and clinical ones are 10.01 ± 11.18% and 5.68 ± 19.82% for the CW and AH, respectively. While the average relative error values are in an acceptable range, the standard deviation is greater than the respective average. This is due to the high variability in clinical data, which can have standard deviations as high as 13%, 16% and 37% from the average value for the AP diameter, CW

and AH, respectively (Mihaila et al., 2014). Despite this, the trend provided by the Golden Proportion agrees with the clinical data.

3.2.2 Leaflet lengths

A recent study showed good correlations between the AP diameter and leaflet lengths (both correlations with $R^2 = 0.94$, p-value = 0.01) (Deorsola and Bellone, 2019). Further adult and paediatric *in vivo* data was retrieved from the literature and compared with the predictions provided by the Golden Proportion, as observed in Figure 10. All adult patient data retrieved from Deorsola *et al.* (2019) (Deorsola and Bellone, 2019) is above the predicted Golden Proportion means; nonetheless, this data comes from a unique study and may have had an associated propagation error at the time of measurements, causing an overestimation of leaflet lengths from clinical images. The Golden Proportion equations do appear able to predict leaflet lengths from the AP diameter, with *in vivo* data falling within the predicted range and R-squared values being 0.89 and 0.69 for anterior (AL) and posterior (PL) leaflet lengths, respectively. Mean relative errors between predicted values and clinical measures are 7.74% and 9.01% for AL and PL lengths, respectively.

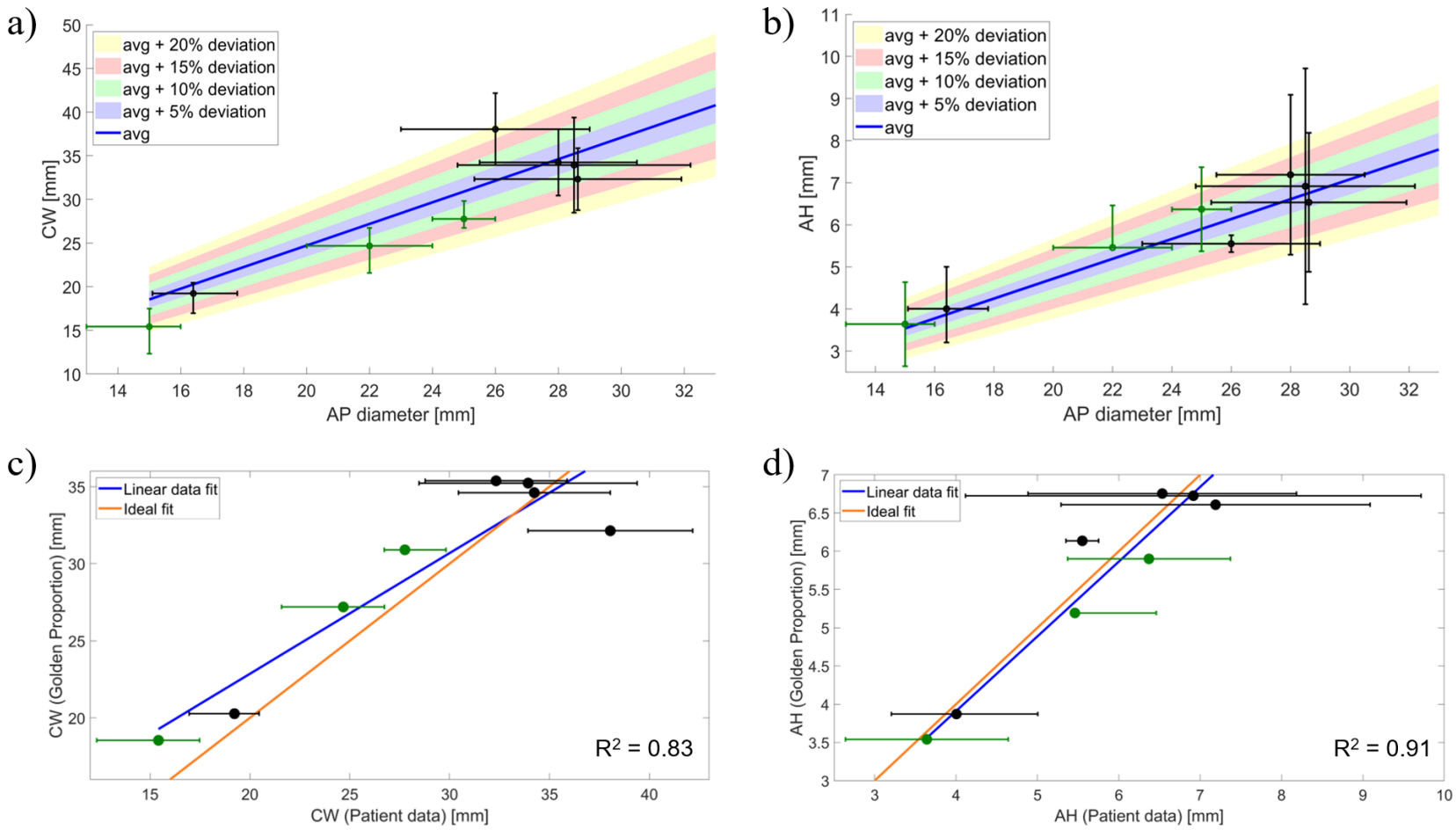

412

413 Figure 9. Predictions for commissural width (a) and annular height (b) as a function of the anteroposterior diameter, as given by the Golden Proportion (colored shades
414 representing up to 20% deviation from the average value) and by adult and paediatric clinical data (represented by black – adult - and dark green – paediatric - standard
415 deviation bars) (Pouch et al., 2014, Jassar et al., 2014, Lee et al., 2013, Mihaila et al., 2014, Jolley et al., 2017, Munin et al., 2014). A direct regression analysis is shown for
416 commissural width (c) and annular height (d), with the orange fitting line representing the one-to-one fit between predicted and patient data and the blue line representing the
417 patient data best linear fit.

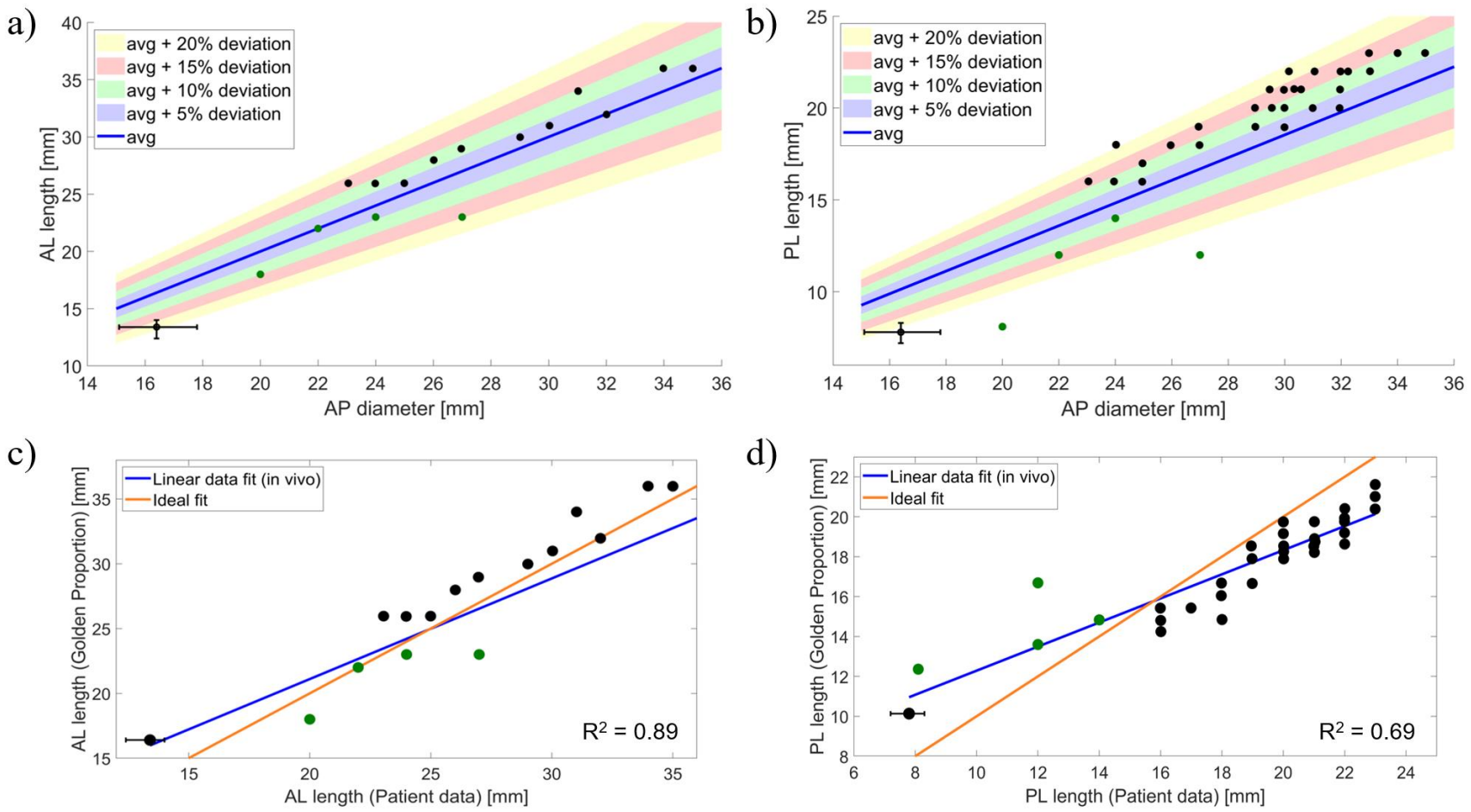

Figure 10. Predictions for anterior (a) and posterior (b) leaflet lengths as a function of the anteroposterior diameter, as given by the Golden Proportion (colored shades representing up to 20% deviation from the average value) and by adult *in vivo* data (Deorsola and Bellone, 2019, Munin et al., 2014). Black and green points represent unique patient data for the studies from Deorsola *et al.* (2019) (Deorsola and Bellone, 2019) and Nomura *et al.* (Nomura et al., 2019), respectively. A direct regression analysis is shown for anterior (c) and posterior (d) leaflet lengths, with the orange fitting line representing the one-to-one fit between predicted and patient data and the blue line representing the patient data best linear fit.

3.2.3 Leaflet areas

The equations for leaflet areas, based on the Golden Proportion, yield total anterior and posterior leaflet areas; therefore, to assess their accuracy in obtaining leaflet surface areas, a comparison against mean total leaflet area values reported in the literature was performed. When total leaflet area values were available, corresponding to diastole, these were directly employed; however, most clinical studies report mean leaflet area values at mid-systole, a time frame where the leaflets are in full coaptation, with the coapting area not being included in the data. Therefore, to enable a comparison to be compatible between our predictions and literature, mean diastolic leaflet areas have been estimated from mean mid-systolic values.

For this estimation, the ratio between the diastolic total leaflet area and the closed mid-systolic leaflet area (minimal area that needs to be covered by the leaflets to occlude the mitral orifice) was employed as a scaling factor. This ratio ranges from 1.4 ± 0.1 (Beaudoin et al., 2013a, Beaudoin et al., 2013b) to 1.63 ± 0.17 (Kim et al., 2019). Here, two ratios of 1.48 and 1.64 were employed to (1) obtain an estimation of the total leaflet areas from adult and paediatric mid-systolic data reported by clinical papers and (2) assess the effect of varying this ratio in the estimation of total leaflet area. An assessment of the average relative errors is presented in Table 1, and predictions for AL and PL surface areas, as provided in the literature and derived from the Golden Proportion, can be observed in Figures 9 and 10.

Table 1. Mean relative difference between Golden Proportion predictions and original mid-systolic data from the literature, as well as estimated diastolic literature data for AL and PL areas, assuming total to closed leaflet surface area ratios of 1.48 and 1.64.

	***In vivo* relative error [%]**		
	Original literature data	**Estimated diastolic data: Ratio = 1.48**	**Estimated diastolic data: Ratio = 1.64**
AL area	84.06	35.61 ± 31.60	23.83 ± 28.65
PL area	73.21	24.39 ± 36.70	13.58 ± 33.25

Table 1 shows that the relative difference between Golden Proportion predictions and original mid-systolic data for leaflet areas is much greater than when comparing Golden Proportion predictions and estimated diastolic data. This further corroborates the fact that estimating diastolic leaflet surface areas is required to assess the validity of the Golden Proportion

predictions. Moreover, the relative error estimated is sensitive to the ratio used, with the average *in vivo* relative error decreasing by more than 10% for both leaflets when the ratio is increased. This ratio greatly varies amongst the AL and PL, since the literature shows ratios of 1.32 ± 0.39 and 1.47 ± 0.50 for AL and PL areas, respectively, for an AP diameter of 14.3 ± 1.8 mm (Debonnaire et al., 2015). In addition, the standard deviation for leaflet surface areas can be as high as 28% for the AL or 25% for the PL in a clinical sample (Mihaila, 2013), which can help justify the elevated variability in literature data and in the resulting error standard deviations present in Table 1.

Figures 11 and 12 show that the *in vivo* data follows the general trend presented by the Golden Proportion predictions for leaflet surface areas, given the assumed percentage of deviation. R-squared values improve with an increasing ratio (AL: 0.34 vs 0.70; PL: 0.15 vs 0.63), suggesting that the Golden Proportion better predicts leaflet surface areas with higher values.

Given these factors, we deemed that a 15 % range for the Golden Proportion prediction of the leaflet areas is acceptable, and, in the toolbox, a value within that range will be employed for leaflet areas.

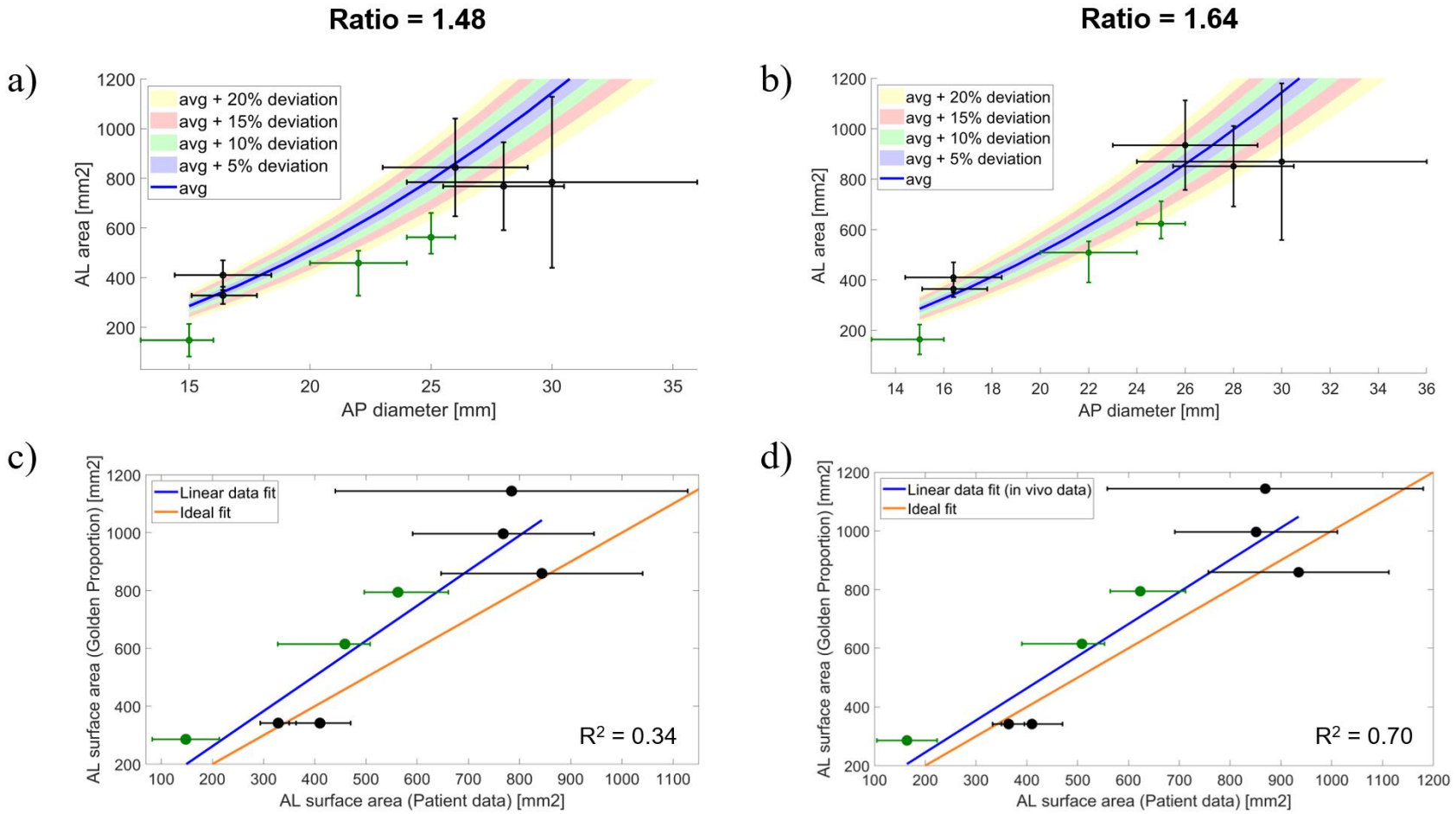

Figure 11. Predictions for the anterior leaflet surface area as a function of the anteroposterior diameter for ratios of 1.48 (a) and 1.64 (b), as given by the Golden Proportion (colored shades representing up to 20% deviation from the average value), by adult and paediatric clinical data (represented by black – adult - and dark green – paediatric - standard deviation bars) (Lee et al., 2013, Mihaila, 2013, Mihaila et al., 2014, Jolley et al., 2017, Munin et al., 2014, Kim et al., 2019). A direct regression analysis is shown for ratios of 1.48 (c) and 1.64 (d), with the orange fitting line representing the one-to-one fit between predicted and patient data and the blue line representing the patient data best linear fit.

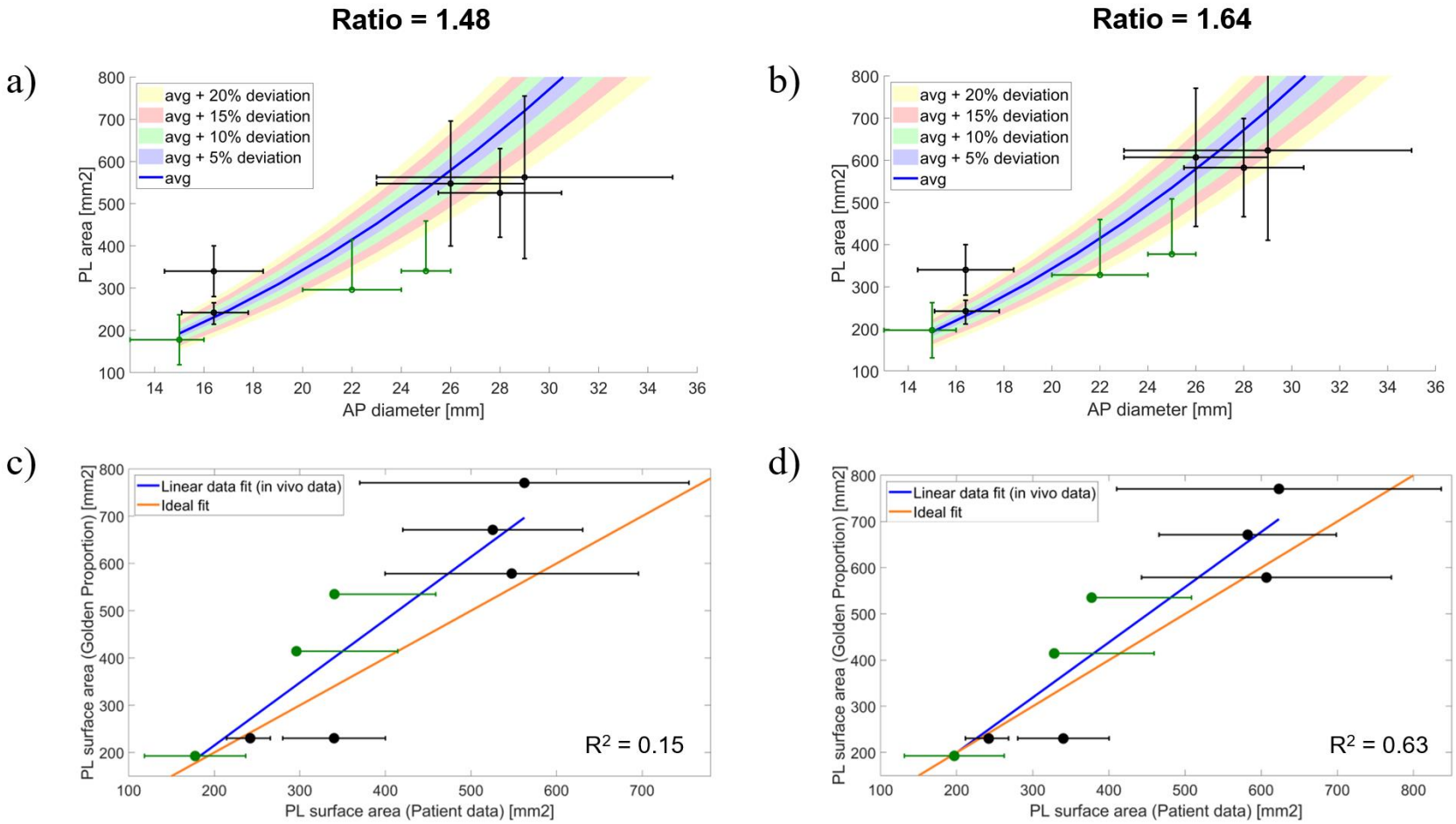

Figure 12. Predictions for the posterior leaflet surface area as a function of the anteroposterior diameter for ratios of 1.48 (a) and 1.64 (b), as given by the Golden Proportion (colored shades representing up to 20% deviation from the average value), by adult and paediatric clinical data (represented by black – adult - and dark green – paediatric - standard deviation bars) (Lee et al., 2013, Mihaila, 2013, Mihaila et al., 2014, Jolley et al., 2017, Munin et al., 2014, Kim et al., 2019). A direct regression analysis is shown for ratios of 1.48 (c) and 1.64 (d), with the orange fitting line representing the one-to-one fit between predicted and patient data and the blue line representing the patient data best linear fit.

4. Pre-processing of the FE model

The final geometrical model created by the MV toolbox corresponds to point cloud boundaries representing the annulus and the free edge. Using functions from the GIBBON toolbox (Moerman, 2018), a surface mesh is created between these boundaries: if the user wishes to export the leaflet mesh as an .stl file, triangular shell elements are chosen; alternatively, if a simulation input file is required, quadrangular shell elements are selected. Complete details on the mesh quality evaluations performed for the quadrangular mesh (ready for LS-DYNA simulations) can be found on Appendix B.

The pre-processing of the geometry to be used in a simulation input file is performed by adding transition elements on the leaflet free edge and creating the chordae tendineae. In LS-DYNA, chordae are discretized into beam elements (two nodes per element), combined with cable material properties, in effect transforming these elements into elastic rods which have resistance under tension, but not under compression. To better represent the movement of the chordae tendineae, each chorda branch is discretized with 6 beam elements. Moreover, two transition quadrangular shell elements are defined at each leaflet insertion point, in continuity with the leaflet free edge shell elements. These transition elements, assumed to consist of a much stiffer material than the leaflet tissue, are where chordae insert, serving to avoid local mesh warping due to the transfer of concentrated loads from chordae tendineae to leaflets (Stevanella et al., 2009). An example of the transition elements added to the model is displayed in Figure 13.

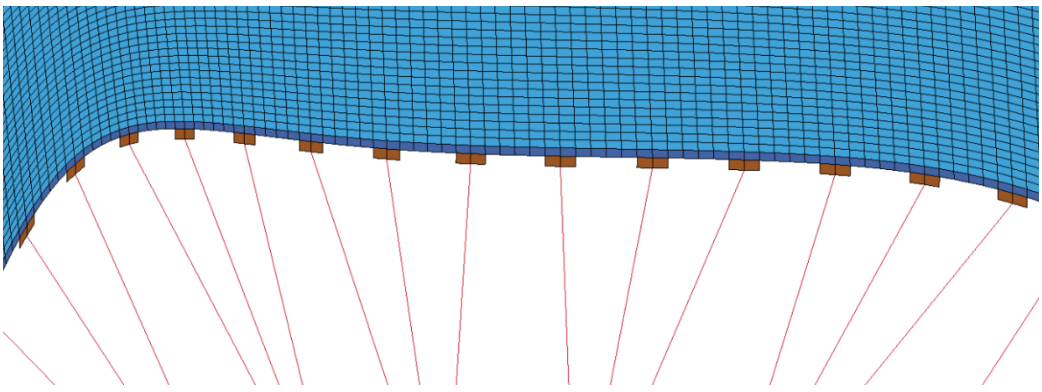

Figure 13. Transition elements on the free margin (brown quadrangular shell elements).

5. Toolbox generated models: examples

A range of average and patient-specific geometries generated by the toolbox are displayed in Figures 14-18 (see Appendix C for more examples of patient-specific creations). Figure 14 shows two average MV shapes obtained from different values for the AP diameter, where a greater value (30 mm) leads to greater leading dimensions governing the annulus and the leaflets when compared with a smaller value (20 mm).

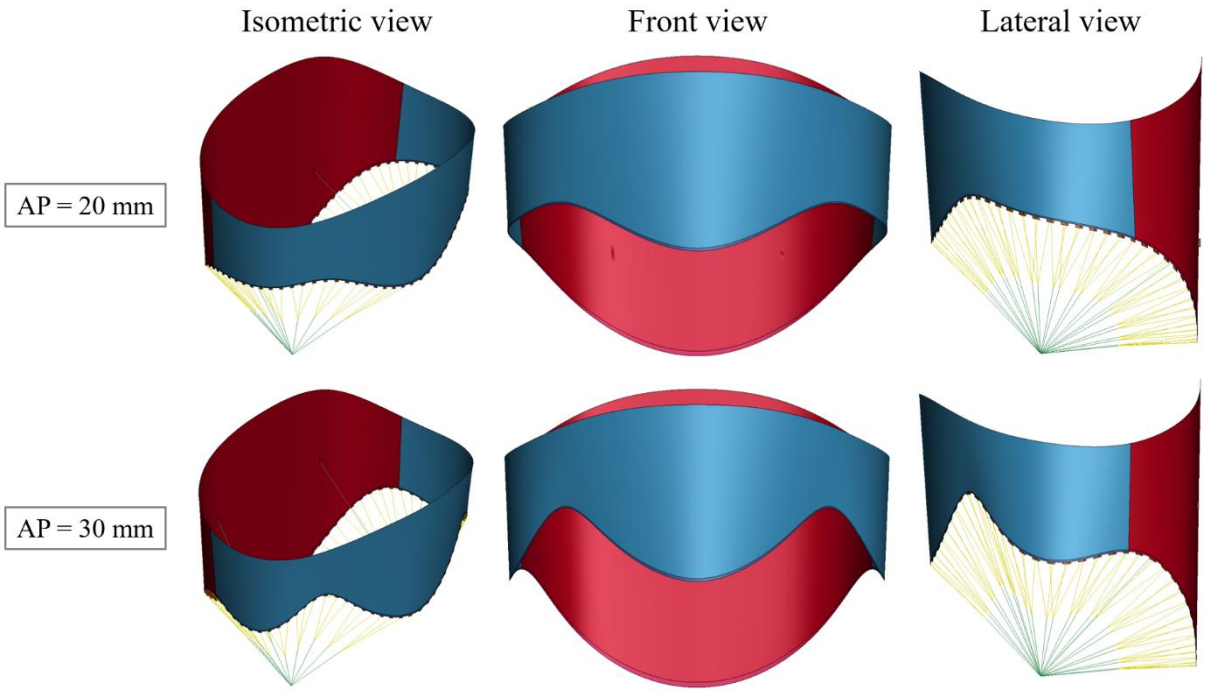

Figure 14. Average MV models generated with different AP diameters (20 and 30 mm).

Figures 15-17 show a range of geometries obtained with varying geometrical parameters individually while keeping others constant. With an increasing AP diameter, the MV annular shape tends to become more circular in shape (Figure 15). Moreover, a greater AL length leads to changes in the AL free edge profile (Figure 16) and an increased PL surface area leads to a broader PL shape (Figure 17). Apart from annular and leaflet dimensions, PM positions can also be prescribed. Figure 18 displays an example of PMPM displacement, a geometric alteration usually associated with impaired performance of the MV. Indeed, the toolbox offers flexibility to generate any desired shape: Appendix D includes LS-DYNA simulation results for average and patient-specific MV models, where the latter is a representation of a diseased valve.

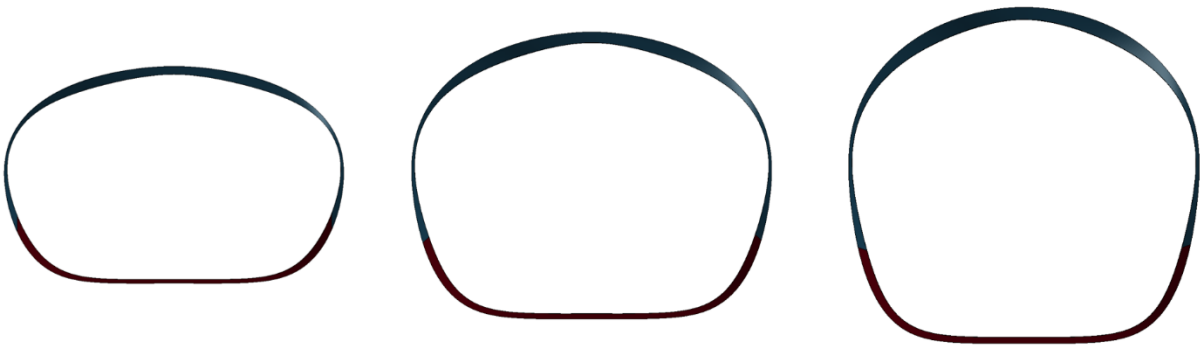

Figure 15. Mitral valve geometry obtained with the AP diameter varying between 20 and 30 mm.

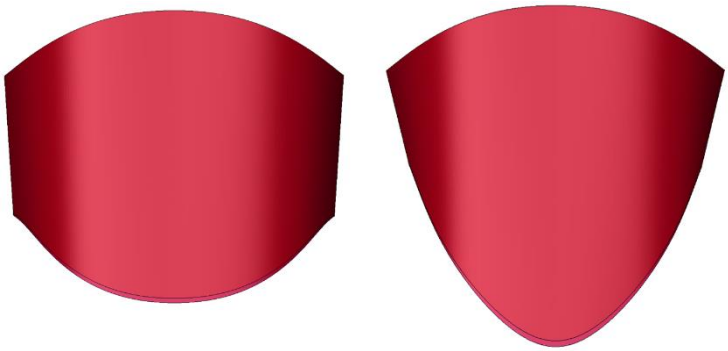

Figure 16. Mitral valve anterior leaflet geometry obtained for anterior leaflet lengths of 25 and 30 mm.

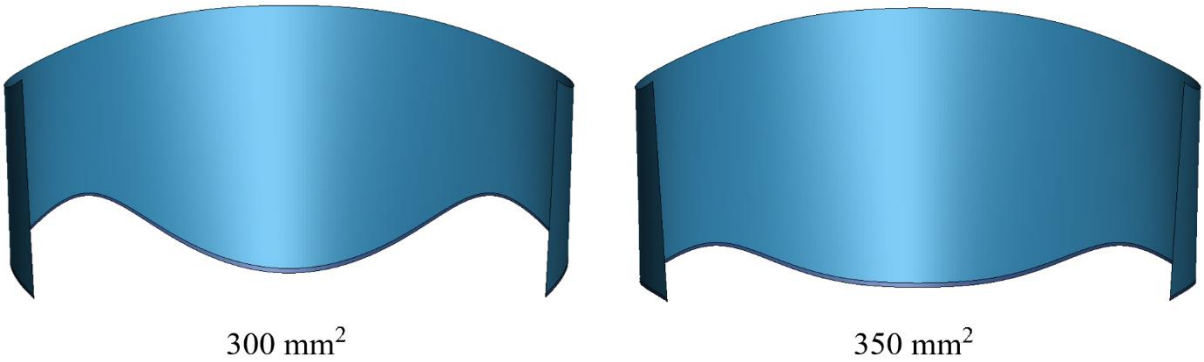

Figure 17. Mitral valve posterior leaflet geometry obtained for posterior leaflet areas varying between 300 and 350 mm^2.

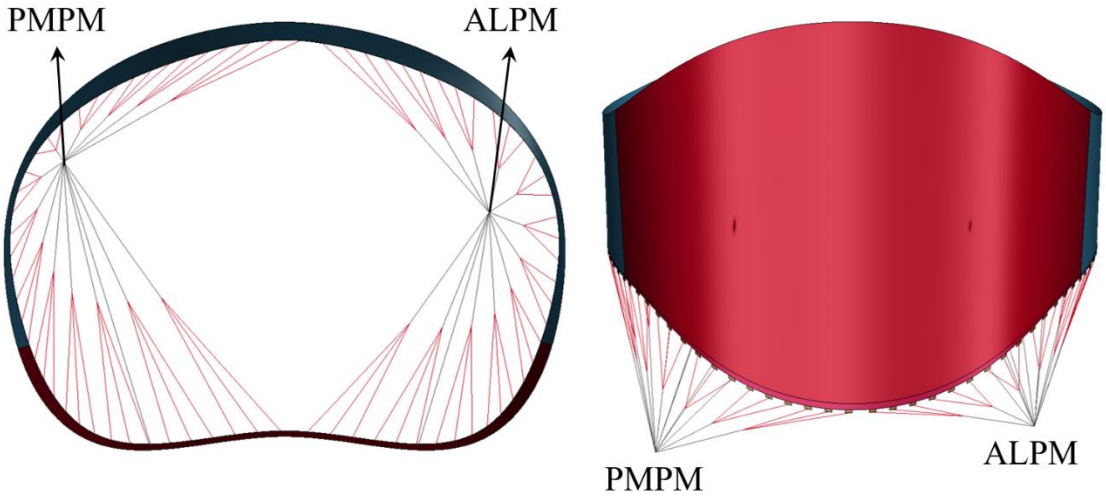

Figure 18. Patient-specific input of PM position, with PMPM displacement represented.

6. Discussion

The MV toolbox allows for the automated and user-controlled generation of tailored MV geometries from patient dimensions, and the creation of finite element input files for computational biomechanical evaluation using minutes of computational time. The main novelty behind this toolbox is that it allows to: (1) obtain a geometrical model, based on dimensions from patient-specific imaging or on predicted values from Golden Proportion equations; (2) create a meshed model which can be pre-processed directly in MATLAB and (3) generate an input file for computational simulations using LS-DYNA.

6.1 Computational approach for the average MV model and current challenges

The average healthy MV shape obtained with the toolbox is based on clinical and *ex vivo* data, and the models generated appear anatomically realistic, being comparable to average (Choi et al., 2016, Alleau et al., 2019) and patient-specific (Stevanella et al., 2011, Pham et al., 2017) models employed in other computational studies. Despite the high average relative errors of the Golden Proportion predictions for leaflet areas against average *in vivo* data (Section 3.2.3), very good correlations (R^2 = 0.94, p-value = 0.01) have been found between MV leaflet lengths and the AP diameter which agreed with the Golden Proportion (Deorsola and Bellone, 2018, Deorsola and Bellone, 2019). Moreover, all annular dimensions

from the literature have also shown agreement with Golden Proportion predictions (Section 3.2.1).

In reality, MV quantitative data is associated with high variability amongst a population sample, as observed in the standard deviations from clinical data. The current limitations present in clinical imaging modalities may directly impact the derived MV morphometric data, contributing towards model uncertainty (Wu and Takeuchi, 2017). In fact, the accuracy of the measurements obtained from scans (especially leaflet areas, which need to be inferred from 3D imaging parameterizations) depend on the type of modality used, their spatial and temporal resolutions, and the operator expertise, which can introduce a bias on the obtained data. Therefore, both the variability in data and the range of accuracy of the measurements present in literature studies can help explain the elevated average relative errors obtained in this study and the standard deviation of those errors. Nonetheless, further studies are required to obtain more complete datasets of morphological measurements of the MV, which lack in the current literature. These can then be used to further validate the Golden Proportion predictions and evaluate new correlation analyses.

The main current challenge of the MV toolbox is the representation of the subvalvular apparatus: even though it is based on the literature (Yamaura, 2008, Sakai et al., 1999), studies describing the PM positioning in the 3D space with greater accuracy are required. Besides, current *in vivo* imaging modalities are unable to properly capture the chordae and the PM (Gao et al., 2017b), and therefore our mathematical representation and distribution of the same is based on such assumptions. This, however, does not differ from computational studies employing average mitral leaflet geometries (Choi et al., 2016, Alleau et al., 2019) and even patient-specific (Gao et al., 2017a, Biffi et al., 2019) ones, since patient-specific chordal distributions are very difficult to obtain.

6.2 Comparison with other state-of-the-art methodologies

Recent studies have either 1) focused on the use of patient-specific models with valvular geometries, material properties and boundary conditions obtained from clinical data, or 2) the development of computational methodologies for the parameterization of the MV structure. While the first approach is time consuming, requiring extensive pre-processing to reconstruct the MV shape of a subject and define patient-specific modelling properties, the second approach is faster, arising as one step forward towards the clinical translation of MV models. Recent parameterization frameworks include the 2D mapping of leaflet surfaces from

imaging modalities for a more intuitive detection of pathology during decision making (Lichtenberg et al., 2020), the creation of 3D MV shapes from specific measurements performed in imaging modalities and their use to study the effect of transcatheter MV replacement in left ventricular outflow tract haemodynamics (Pasta et al., 2020), and a heuristic generation of chordae tendineae and PM tips (Walczak et al., 2021). While these frameworks are able to quickly generate clinically relevant MV shapes, they can only be applied to individual cases. The MV toolbox, on the other hand, is flexible, enabling the creation of morphological MV models, scalable to average human dimensions or patient-specific ones, within a timescale compatible with clinical use. In addition, the models can be directly meshed and an input file including material properties, boundary conditions and contact conditions, ready for computational simulations, can be outputted. The toolbox generates meshed models which meet criteria for numerical modelling. This means that the model pre-processing can be accelerated further, since it can be directly set up for computational simulations without other tiresome processes. As far as the authors know, our study is the first MV parametric model which allows the variation of its anatomy and has the flexibility to input the dimensions of a specific subject; subsequently generating an input file ready for numerical analysis (Figure 19).

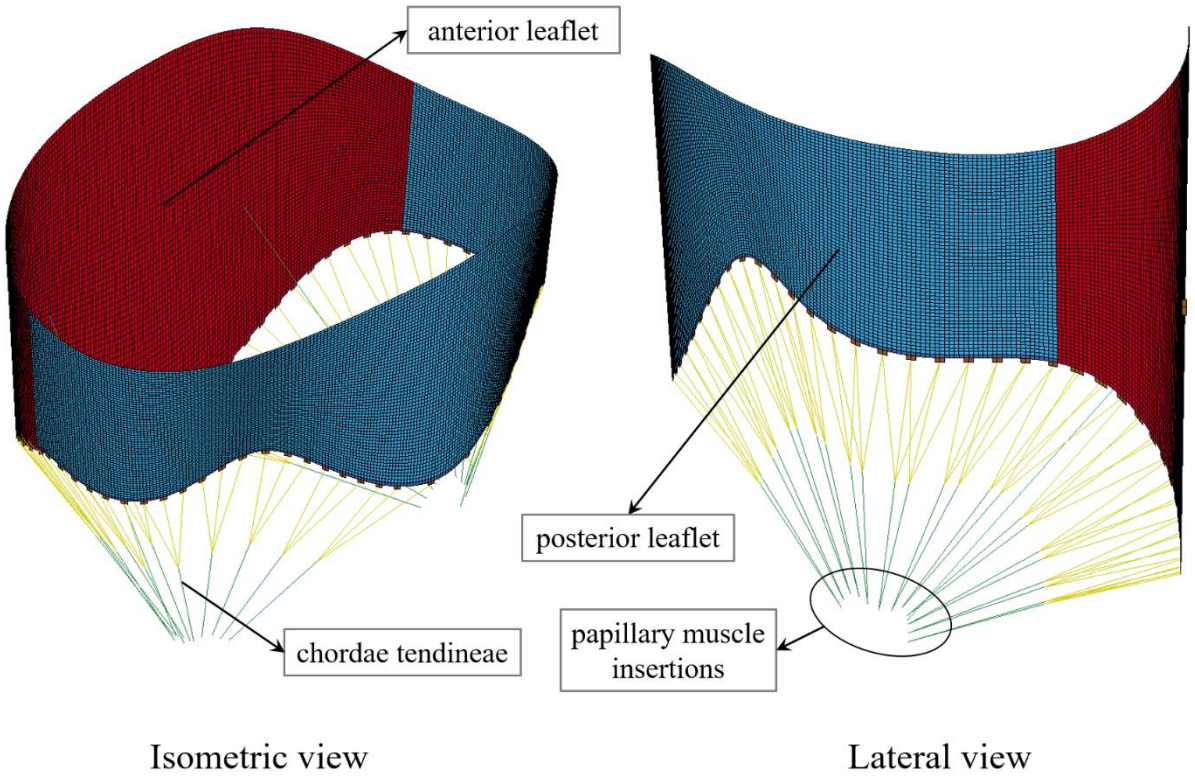

Figure 19. Sample 3D MV model with all components included, ready for computational simulations.

6.3 Potential applications

The MV toolbox can have several end-user applications. From a clinical perspective, and given its flexibility, it can be used to study the influence of morphological MV parameters on its function. The average MV shape generated assumes a healthy valve, and degenerative valve disease, for instance, leads to significant alteration in mitral valve proportions (Deorsola and Bellone, 2019). However, inputted patient-specific parameters can be used to create a range of diseased scenarios, such as: varying annular diameters to represent different cases of annular dilation (Kim et al., 2019, Lee et al., 2013), which can compromise leaflet coaptation (Ito et al., 2017); incorporating PM displacement, which is well correlated with increased regurgitant volume in patients with functional ischemic mitral regurgitation (Obase et al., 2016, Ito et al., 2017); or increasing leaflet surface area to represent myxomatous degeneration of the MV (Clavel et al., 2015). Moreover, clinicians can use the toolbox to virtually evaluate current and novel mitral interventions, such as the use of extension biological patches to restore leaflet dimensions in the case of posterior leaflet congenital hypoplasia (Parato and Masia, 2018), or papillary muscle approximation as an adjunctive technique for MV regurgitation (Mihos et al., 2017). The toolbox can be further edited to allow for the inclusion of medical devices (such as annuloplasty rings (Kong et al., 2018)) and virtually assess their performance and influence on the biomechanics of the MV using a range of MV models through computational simulations. Ultimately, this could aid with the design optimization and customization of new devices.

6.4 Future work

This study has focused on the concept of developing a framework for the automated generation of geometrical models of the MV. This model is to be developed further, especially concerning the representation of the subvalvular apparatus: greater control on the addition process of the chordae tendineae, including the possibility of choosing different branching numbers and insertion into different portions of the leaflets, shall be implemented. Moreover, the possibilities of output for computational simulations will be extended: in addition to the already implemented ready-to-use LS-DYNA mesh, the code will be expanded to allow for output of the MV model in formats compatible with other software such as gmsh or VTK. The output for computational simulations will also be further developed: material properties will be improved by implementing a leaflet hyperelastic tissue model accounting for collagen fiber orientation. This will include using a layered shell

composite model (Wenk et al., 2010, Wenk et al., 2012). More realistic kinematic boundary conditions will be implemented to accurately represent annular contraction and PM motion. Different PM movements during the cardiac cycle will also be tested in future studies. Finally, focus will be given to the development of a fluid-structure interaction model, to account for the passage of blood through the valve and its interaction with the leaflet tissue (Gao et al., 2017a, Huang et al., 2021). The development version of the toolbox is freely available on GitHub and its future release will be provided with a more complete GUI and pre-processing features as mentioned above.

7. Conclusion

The MV toolbox has been developed with the aim of studying the influence of morphological MV parameters on its function, including diseased configurations, and to virtually evaluate diverse mitral interventions at a customised level. The toolbox enables an automated and user independent workflow which is compatible with a range of modelling software. Together with biomedical engineering professionals, clinicians could use this tool to simulate and understand how different MV patient-specific morphometries can impact valve biomechanics. Moreover, clinicians will have a choice on whether to use average dimensions or provide dimensions from imaging data as an input. It can then be employed to aid clinicians when assessing MV biomechanics of their patients and improve the decision-making process behind choosing the best patient-specific clinical intervention.

Data accessibility: The full source code of the toolbox has been released on Zenodo (DOI: 10.5281/zenodo.5018364), currently with restricted access (de Oliveira, 2021). The intention is for it to be made publicly available if the manuscript is accepted. The protected link for access (expiring on 24th July 2021) is:
https://zenodo.org/record/5018364?token=eyJhbGciOiJIUzUxMiIsImV4cCI6MTYyNzA3NzU5OSwiaWF0IjoxNjI0NDYxMDk4fQ.eyJkYXRhIjp7InJlY2lkIjo1MDE4MzY0fSwiaWQiOjE1NzYwLCJybmQiOiIwOGVmZWRiNSJ9.s7azvCQRiPNSa-H3UPyYtKs1mNjF5bH6RXzWcn-m9jPMtrnFz_hRz_zjagdJ0_N6vbRV4RTY0fhU2qbEzRchKQ

Funding: This research did not receive any specific grant from funding agencies in the public, commercial, or not-for-profit sectors.

References

AGUILERA, H. M., URHEIM, S., SKALLERUD, B. & PROT, V. 2021. Influence of Annular Dynamics and Material Behavior in Finite Element Analysis of Barlow's Mitral Valve Disease. *Journal of Elasticity*.

AL-ATABI, M., ESPINO, D. M., HUKINS, D. W. & BUCHAN, K. G. 2012. Biomechanical assessment of surgical repair of the mitral valve. *Proc Inst Mech Eng H,* 226**,** 275-87.

ALLEAU, T., LANQUETIN, L. & SALSAC, A. V. 2019. Use of a parametric finite element model of the mitral valve to assess healthy and pathological valve behaviors. *Computer Methods in Biomechanics and Biomedical Engineering,* 22**,** S4-S5.

BEAUDOIN, J., HANDSCHUMACHER, M. D., ZENG, X., HUNG, J., MORRIS, E. L., LEVINE, R. A. & SCHWAMMENTHAL, E. 2013a. Mitral valve enlargement in chronic aortic regurgitation as a compensatory mechanism to prevent functional mitral regurgitation in the dilated left ventricle. *J Am Coll Cardiol,* 61**,** 1809-16.

BEAUDOIN, J., THAI, W. E., WAI, B., HANDSCHUMACHER, M. D., LEVINE, R. A. & TRUONG, Q. A. 2013b. Assessment of mitral valve adaptation with gated cardiac computed tomography: validation with three-dimensional echocardiography and mechanistic insight to functional mitral regurgitation. *Circ Cardiovasc Imaging,* 6**,** 784-9.

BIAU, D. J., KERNEIS, S. & PORCHER, R. 2008. Statistics in brief: the importance of sample size in the planning and interpretation of medical research. *Clin Orthop Relat Res,* 466**,** 2282-8.

BIFFI, B., GRITTI, M., GRASSO, A., MILANO, E. G., FONTANA, M., ALKAREEF, H., DAVAR, J., JEETLEY, P., WHELAN, C., ANDERSON, S., LORUSSO, D., SAUVAGE, E., MARIA BOSI, G., SCHIEVANO, S. & CAPELLI, C. 2019. A workflow for patient-specific fluid-structure interaction analysis of the mitral valve: A proof of concept on a mitral regurgitation case. *Med Eng Phys,* 74**,** 153-161.

CABALLERO, A., MAO, W., MCKAY, R. & SUN, W. 2020. Transapical mitral valve repair with neochordae implantation: FSI analysis of neochordae number and complexity of leaflet prolapse. *Int J Numer Method Biomed Eng,* 36**,** e3297.

CABALLERO, A., MAO, W. B., MCKAY, R., PRIMIANO, C., HASHIM, S. & SUN, W. 2019. New insights into mitral heart valve prolapse after chordae rupture through fluid-structure interaction computational modeling (vol 8. 17306, 2018). *Scientific Reports,* 9.

CHOI, A., MCPHERSON, D. D. & KIM, H. 2016. Biomechanical evaluation of the pathophysiologic developmental mechanisms of mitral valve prolapse: effect of valvular morphologic alteration. *Med Biol Eng Comput,* 54**,** 799-809.

CHOI, P. S., NAM, H. H., LASSO, A., HERZ, C., DROUIN, S., HARRILD, D. M., QUARTERMAIN, M., FICHTINGER, G., MASCIO, C. E., EMANI, S. & JOLLEY, M. A. 2020. Three-Dimensional Modeling of Surgically Implanted Stent-Based Valves in the Mitral Position in Children. *Ann Thorac Surg,* 110**,** 670-675.

CLAVEL, M. A., MANTOVANI, F., MALOUF, J., MICHELENA, H. I., VATURY, O., JAIN, M. S., MANKAD, S. V., SURI, R. M. & ENRIQUEZ-SARANO, M. 2015. Dynamic phenotypes of degenerative myxomatous mitral valve disease: quantitative 3-dimensional echocardiographic study. *Circ Cardiovasc Imaging,* 8.

CONG, T., GU, J., LEE, A. P., SHANG, Z., SUN, Y., SUN, Q., WEI, H., CHEN, N., SUN, S. & FU, T. 2018. Quantitative analysis of mitral valve morphology in atrial functional mitral regurgitation using real-time 3-dimensional echocardiography atrial functional mitral regurgitation. *Cardiovasc Ultrasound,* 16**,** 13.

DAGUM, P., TIMEK, T., GREEN, G. R., DAUGHTERS, G. T., LIANG, D., INGELS, N. B., JR. & MILLER, D. C. 2001. Three-dimensional geometric comparison of partial and complete flexible mitral annuloplasty rings. *J Thorac Cardiovasc Surg,* 122**,** 665-73.

DE OLIVEIRA, D. C. 2021. Mitral Valve Model Generator: First Release.

DEBONNAIRE, P., AL AMRI, I., LEONG, D. P., JOYCE, E., KATSANOS, S., KAMPERIDIS, V., SCHALIJ, M. J., BAX, J. J., MARSAN, N. A. & DELGADO, V. 2015. Leaflet remodelling in functional mitral valve regurgitation: characteristics, determinants, and relation to regurgitation severity. *Eur Heart J Cardiovasc Imaging,* 16**,** 290-9.

DEGANDT, A. A., WEBER, P. A., SABER, H. A. & DURAN, C. M. 2007. Mitral valve basal chordae: comparative anatomy and terminology. *Ann Thorac Surg,* 84**,** 1250-5.

DEORSOLA, L. & BELLONE, A. 2018. Coaptation Triangle and Golden Proportion in mitral valve anatomy. Does nature play with geometry? *Echocardiography,* 35**,** 30-38.

DEORSOLA, L. & BELLONE, A. 2019. The Golden Proportion in the scallop geometry of normal mitral valves. When nature plays with jigsaw puzzles. *Echocardiography,* 36**,** 1028-1034.

DI DONATO, M., DABIC, P., CASTELVECCHIO, S., SANTAMBROGIO, C., BRANKOVIC, J., COLLARINI, L., JOUSSEF, T., FRIGIOLA, A., BUCKBERG, G., MENICANTI, L. & GROUP, R. 2006. Left ventricular geometry in normal and post-anterior myocardial infarction patients: sphericity index and 'new' conicity index comparisons. *Eur J Cardiothorac Surg,* 29 Suppl 1**,** S225-30.

DOLL, N., SHEYTANOV, V., LABROUSSE, L., CHU, M. W. A., STEFANO, P., MOKRACEK, A., BARON, O., LI, S. & GUNZINGER, R. 2019. Clinical performance of a three-dimensional saddle-shaped, rigid ring for mitral valve repair. *Eur J Cardiothorac Surg,* 55**,** 217-223.

DOMENICHINI, F. & PEDRIZZETTI, G. 2015. Asymptotic Model of Fluid-Tissue Interaction for Mitral Valve Dynamics. *Cardiovasc Eng Technol,* 6**,** 95-104.

DOMENICHINI, F., PEDRIZZETTI, G. & BACCANI, B. 2005. Three-dimensional filling flow into a model left ventricle. *J Fluid Mech,* 539**,** 179–198.

DUPLESSIS, L. A. & MARCHAND, P. 1964. The Anatomy of the Mitral Valve and Its Associated Structures. *Thorax,* 19**,** 221-7.

ESPINO, D. M., SHEPHERD, D. E. & BUCHAN, K. G. 2007. Effect of mitral valve geometry on valve competence. *Heart Vessels,* 22**,** 109-15.

FERRING, V. & PANCHERZ, H. 2008. Divine proportions in the growing face. *Am J Orthod Dentofacial Orthop,* 134**,** 472-9.

GAO, H., FENG, L., QI, N., BERRY, C., GRIFFITH, B. E. & LUO, X. 2017a. A coupled mitral valve-left ventricle model with fluid-structure interaction. *Med Eng Phys,* 47**,** 128-136.

GAO, H., QI, N., FENG, L., MA, X., DANTON, M., BERRY, C. & LUO, X. 2017b. Modelling mitral valvular dynamics-current trend and future directions. *Int J Numer Method Biomed Eng,* 33.

HENEIN, M. Y., GOLDEN RATIO, C., ZHAO, Y., NICOLL, R., SUN, L., KHIR, A. W., FRANKLIN, K. & LINDQVIST, P. 2011. The human heart: application of the golden ratio and angle. *Int J Cardiol,* 150**,** 239-42.

HUANG, X. Y., DENG, L., ZUO, H., YANG, C., SONG, Y. H., LESPERANCE, M. & TANG, D. L. 2021. Comparisons of simulation results between passive and active fluid structure interaction models for left ventricle in hypertrophic obstructive cardiomyopathy. *Biomed Eng Online,* 20.

IOSA, M., FUSCO, A., MARCHETTI, F., MORONE, G., CALTAGIRONE, C., PAOLUCCI, S. & PEPPE, A. 2013. The golden ratio of gait harmony: repetitive proportions of repetitive gait phases. *Biomed Res Int,* 2013**,** 918642.

ITO, K., ABE, Y., TAKAHASHI, Y., SHIMADA, Y., FUKUMOTO, H., MATSUMURA, Y., NARUKO, T., SHIBATA, T., YOSHIYAMA, M. & YOSHIKAWA, J. 2017. Mechanism of atrial functional mitral regurgitation in patients with atrial fibrillation: A study using three-dimensional transesophageal echocardiography. *J Cardiol,* 70**,** 584-590.

JASSAR, A. S., VERGNAT, M., JACKSON, B. M., MCGARVEY, J. R., CHEUNG, A. T., FERRARI, G., WOO, Y. J., ACKER, M. A., GORMAN, R. C. & GORMAN, J. H. 2014. Regional Annular Geometry in Patients With Mitral Regurgitation: Implications for Annuloplasty Ring Selection. *Annals of Thoracic Surgery,* 97**,** 64-70.

JIANG, L., OWAIS, K., MATYAL, R., KHABBAZ, K. R., LIU, D. C., MONTEALEGRE-GALLEGOS, M., HESS, P. E. & MAHMOOD, F. 2014. Dynamism of the mitral annulus: a spatial and temporal analysis. *J Cardiothorac Vasc Anesth,* 28**,** 1191-7.

JOLLEY, M. A., GHELANI, S. J., ADAR, A. & HARRILD, D. M. 2017. Three-Dimensional Mitral Valve Morphology and Age-Related Trends in Children and Young Adults with Structurally Normal Hearts Using Transthoracic Echocardiography. *J Am Soc Echocardiogr,* 30**,** 561-571.

KAISER, A. D., MCQUEEN, D. M. & PESKIN, C. S. 2019. Modeling the mitral valve. *Int J Numer Method Biomed Eng***,** e3240.

KIM, D. H., HEO, R., HANDSCHUMACHER, M. D., LEE, S., CHOI, Y. S., KIM, K. R., SHIN, Y., PARK, H. K., BISCHOFF, J., AIKAWA, E., SONG, J. M., KANG, D. H., LEVINE, R. A. & SONG, J. K. 2019. Mitral Valve Adaptation to Isolated Annular Dilation: Insights Into the Mechanism of Atrial Functional Mitral Regurgitation. *JACC Cardiovasc Imaging,* 12**,** 665-677.

KIM, K., KAJI, S., AN, Y., NISHINO, T., TANI, T., KITAI, T. & FURUKAWA, Y. 2014. Interpapillary muscle distance independently affects severity of functional mitral regurgitation in patients with systolic left ventricular dysfunction. *J Thorac Cardiovasc Surg,* 148**,** 434-40 e1.

KIM, K., KAJI, S., AN, Y., YOSHITANI, H., TAKEUCHI, M., LEVINE, R. A., OTSUJI, Y. & FURUKAWA, Y. 2012. Mechanism of asymmetric leaflet tethering in ischemic mitral regurgitation: 3D analysis with multislice CT. *JACC Cardiovasc Imaging,* 5**,** 230-2.

KOHLI, K., WEI, Z. A., SADRI, V., NETTO, T., LISKO, J. C., GREENBAUM, A. B., BABALIAROS, V., OSHINSKI, J. N. & YOGANATHAN, A. P. 2021. A Simplified In Silico Model of Left Ventricular Outflow in Patients After Transcatheter Mitral Valve Replacement with Anterior Leaflet Laceration. *Ann Biomed Eng,* 49**,** 1449-1461.

KONG, F., CABALLERO, A., MCKAY, R. & SUN, W. 2020. Finite element analysis of MitraClip procedure on a patient-specific model with functional mitral regurgitation. *J Biomech,* 104**,** 109730.

KONG, F., PHAM, T., MARTIN, C., ELEFTERIADES, J., MCKAY, R., PRIMIANO, C. & SUN, W. 2018. Finite element analysis of annuloplasty and papillary muscle relocation on a patient-specific mitral regurgitation model. *PLoS One,* 13**,** e0198331.

KRAWCZYK-OZOG, A., HOLDA, M. K., SORYSZ, D., KOZIEJ, M., SIUDAK, Z., DUDEK, D. & KLIMEK-PIOTROWSKA, W. 2017. Morphologic variability of the mitral valve leaflets. *J Thorac Cardiovasc Surg,* 154**,** 1927-1935.

LAM, J. H., RANGANATHAN, N., WIGLE, E. D. & SILVER, M. D. 1970. Morphology of the human mitral valve. I. Chordae tendineae: a new classification. *Circulation,* 41**,** 449-58.

LEE, A. P., HSIUNG, M. C., SALGO, I. S., FANG, F., XIE, J. M., ZHANG, Y. C., LIN, Q. S., LOOI, J. L., WAN, S., WONG, R. H., UNDERWOOD, M. J., SUN, J. P., YIN, W. H., WEI, J., TSAI, S. K. & YU, C. M. 2013. Quantitative analysis of mitral valve morphology in mitral valve prolapse with real-time 3-dimensional echocardiography: importance of annular saddle shape in the pathogenesis of mitral regurgitation. *Circulation,* 127**,** 832-41.

LEVACK, M. M., JASSAR, A. S., SHANG, E. K., VERGNAT, M., WOO, Y. J., ACKER, M. A., JACKSON, B. M., GORMAN, J. H., 3RD & GORMAN, R. C. 2012. Three-dimensional echocardiographic analysis of mitral annular dynamics: implication for annuloplasty selection. *Circulation,* 126**,** S183-8.

LICHTENBERG, N., EULZER, P., ROMANO, G., BRCIC, A., KARCK, M., LAWONN, K., DE SIMONE, R. & ENGELHARDT, S. 2020. Mitral valve flattening and parameter mapping for patient-specific valve diagnosis. *Int J Comput Assist Radiol Surg,* 15**,** 617-627.

MAFFESSANTI, F., GRIPARI, P., PONTONE, G., ANDREINI, D., BERTELLA, E., MUSHTAQ, S., TAMBORINI, G., FUSINI, L., PEPI, M. & CAIANI, E. G. 2013. Three-dimensional dynamic assessment of tricuspid and mitral annuli using cardiovascular magnetic resonance. *Eur Heart J Cardiovasc Imaging,* 14**,** 986-95.

MIHAILA, S., MURARU, D., PIASENTINI, E., MIGLIORANZA, M. H., PELUSO, D., CUCCHINI, U., ILICETO, S., VINEREANU, D. & BADANO, L. P. 2014. Quantitative analysis of mitral annular geometry and function in healthy volunteers using transthoracic three-dimensional echocardiography. *J Am Soc Echocardiogr,* 27**,** 846-57.

MIHAILA, S., MURARU, D., CASABLANA, S., PELUSO, D., CUCCHINI, U., DEL BIANCO, L., VINEREANU, D., ILICETO, S., BADANO, L. 2013. Three-dimensional changes in mitral valve annulus geometry in organic and functional mitral regurgitation: insights for mitral valve repair. *Eur. Heart J.,* 34**,** 4751.

MIHOS, C. G., YUCEL, E. & SANTANA, O. 2017. The role of papillary muscle approximation in mitral valve repair for the treatment of secondary mitral regurgitation. *Eur J Cardiothorac Surg,* 51**,** 1023-1030.

MISFELD, M. & SIEVERS, H. H. 2007. Heart valve macro- and microstructure. *Philos Trans R Soc Lond B Biol Sci,* 362**,** 1421-36.

MOERMAN, K. M. 2018. GIBBON: The Geometry and Image-Based Bioengineering add-On. *JOSS,* 3**,** 506.

MUNIN, M. A., THIERER, J., RAGGIO, I. M., GOERNER, M. S., LOMBARDERO, M., GODIA, J., SÁNCHEZ, G. A., SPERNANZONI, F., ORTEGA, J. & TORRES, V. 2014. Three Dimensional Echocardiographic Analysis of Mitral Valve Characteristics. *Rev Argent Cardiol,* 82**,** 279-284.

NCHO, B. E., PIERCE, E. L., BLOODWORTH, C. H. T., IMAI, A., OKAMOTO, K., SAITO, Y., GORMAN, R. C., GORMAN, J. H., 3RD & YOGANATHAN, A. P. 2020. Optimized mitral annuloplasty ring design reduces loading in the posterior annulus. *J Thorac Cardiovasc Surg,* 159**,** 1766-1774 e2.

NOMURA, K., AJIRO, Y., NAKANO, S., MATSUSHIMA, M., YAMAGUCHI, Y., HATAKEYAMA, N., OHATA, M., SAKUMA, M., NONAKA, T., HARII, M., UTSUMI, M., SAKAMOTO, K., IWADE, K. & KUNINAKA, N. 2019. Characteristics of mitral valve leaflet length in patients with pectus excavatum: A single center cross-sectional study. *PLoS One,* 14**,** e0212165.

OBASE, K., WEINERT, L., HOLLATZ, A., FAROOQUI, F., ROBERTS, J. D., MINHAJ, M. M., TUNG, A., CHANEY, M., OTA, T., JEEVANANDAM, V., YOSHIDA, K., MOR-AVI, V. & LANG, R. M. 2016. Elongation of chordae tendineae as an adaptive process

to reduce mitral regurgitation in functional mitral regurgitation. *Eur Heart J Cardiovasc Imaging,* 17**,** 500-9.
OKAMOTO, H., ITOH, Y. & NARA, Y. 2007. Geometric analysis of the anterior mitral leaflet and mitral valve orifice in cadaveric hearts. *Circ J,* 71**,** 1794-9.
OLIVEIRA, D., SRINIVASAN, J., ESPINO, D., BUCHAN, K., DAWSON, D. & SHEPHERD, D. 2020. Geometric description for the anatomy of the mitral valve: A review. *J Anat,* 237**,** 209-224.
PARATO, V. M. & MASIA, S. L. 2018. Hypoplasia or Absence of Posterior Leaflet: A Rare Congenital Anomaly of The Mitral Valve in Adulthood - Case Series. *J Cardiovasc Echogr,* 28**,** 45-47.
PARK, J., GEIRSSON, A. & BONDE, P. N. 2019. Mathematical Blueprint of a Mitral Valve. *Semin Thorac Cardiovasc Surg*.
PASTA, S., CANNATA, S., GENTILE, G., AGNESE, V., PILATO, M. & GANDOLFO, C. 2020. Simulation of left ventricular outflow tract (LVOT) obstruction in transcatheter mitral valve-in-ring replacement. *Med Eng Phys,* 82**,** 40-48.
PHAM, T., KONG, F., MARTIN, C., WANG, Q., PRIMIANO, C., MCKAY, R., ELEFTERIADES, J. & SUN, W. 2017. Finite Element Analysis of Patient-Specific Mitral Valve with Mitral Regurgitation. *Cardiovasc Eng Technol,* 8**,** 3-16.
POUCH, A. M., VERGNAT, M., MCGARVEY, J. R., FERRARI, G., JACKSON, B. M., SEHGAL, C. M., YUSHKEVICH, P. A., GORMAN, R. C. & GORMAN, J. H. 2014. Statistical Assessment of Normal Mitral Annular Geometry Using Automated Three-Dimensional Echocardiographic Analysis. *Annals of Thoracic Surgery,* 97**,** 71-77.
RANGANATHAN, N., LAM, J. H., WIGLE, E. D. & SILVER, M. D. 1970. Morphology of the human mitral valve. II. The valve leaflets. *Circulation,* 41**,** 459-67.
SAHA, A. & ROY, S. 2018. Papillary muscles of left ventricle-Morphological variations and it's clinical relevance. *Indian Heart J,* 70**,** 894-900.
SAKAI, T., OKITA, Y., UEDA, Y., TAHATA, T., OGINO, H., MATSUYAMA, K. & MIKI, S. 1999. Distance between mitral anulus and papillary muscles: anatomic study in normal human hearts. *J Thorac Cardiovasc Surg,* 118**,** 636-41.
SALGO, I. S., GORMAN, J. H., 3RD, GORMAN, R. C., JACKSON, B. M., BOWEN, F. W., PLAPPERT, T., ST JOHN SUTTON, M. G. & EDMUNDS, L. H., JR. 2002. Effect of annular shape on leaflet curvature in reducing mitral leaflet stress. *Circulation,* 106**,** 711-7.
SHEN, X., WANG, T., CAO, X. & CAI, L. 2017. The geometric model of the human mitral valve. *PLoS One,* 12**,** e0183362.
STEVANELLA, M., MAFFESSANTI, F., CONTI, C. A., VOTTA, E., ARNOLDI, A., LOMBARDI, M., PARODI, O., CAIANI, E. G. & REDAELLI, A. 2011. Mitral Valve Patient-Specific Finite Element Modeling from Cardiac MRI: Application to an Annuloplasty Procedure. *Cardiovascular Engineering and Technology,* 2**,** 66-76.
STEVANELLA, M., VOTTA, E. & REDAELLI, A. 2009. Mitral valve finite element modeling: implications of tissues' nonlinear response and annular motion. *J Biomech Eng,* 131**,** 121010.
SUN, X., JIANG, Y., HUANG, G., HUANG, J., SHI, M., PANG, L. & WANG, Y. 2019. Three-dimensional mitral valve structure in predicting moderate ischemic mitral regurgitation improvement after coronary artery bypass grafting. *J Thorac Cardiovasc Surg,* 157**,** 1795-1803 e2.
TANG, Z., FAN, Y. T., WANG, Y., JIN, C. N., KWOK, K. W. & LEE, A. P. 2019. Mitral Annular and Left Ventricular Dynamics in Atrial Functional Mitral Regurgitation: A Three-Dimensional and Speckle-Tracking Echocardiographic Study. *J Am Soc Echocardiogr,* 32**,** 503-513.

WALCZAK, L., TAUTZ, L., NEUGEBAUER, M., GEORGII, J., WAMALA, I., SUNDERMANN, S., FALK, V. & HENNEMUTH, A. 2021. Interactive editing of virtual chordae tendineae for the simulation of the mitral valve in a decision support system. *Int J Comput Assist Radiol Surg,* 16**,** 125-132.

WARRAICH, H. J., CHAUDARY, B., MASLOW, A., PANZICA, P. J., PUGSLEY, J. & MAHMOOD, F. 2012. Mitral annular nonplanarity: correlation between annular height/commissural width ratio and the nonplanarity angle. *J Cardiothorac Vasc Anesth,* 26**,** 186-90.

WENK, J. F., RATCLIFFE, M. B. & GUCCIONE, J. M. 2012. Finite element modeling of mitral leaflet tissue using a layered shell approximation. *Med Biol Eng Comput,* 50**,** 1071-1079.

WENK, J. F., ZHANG, Z., CHENG, G., MALHOTRA, D., ACEVEDO-BOLTON, G., BURGER, M., SUZUKI, T., SALONER, D. A., WALLACE, A. W., GUCCIONE, J. M. & RATCLIFFE, M. B. 2010. First finite element model of the left ventricle with mitral valve: insights into ischemic mitral regurgitation. *Ann Thorac Surg,* 89**,** 1546-53.

WU, V. C. & TAKEUCHI, M. 2017. Three-Dimensional Echocardiography: Current Status and Real-Life Applications. *Acta Cardiol Sin,* 33**,** 107-118.

XU, F., JOHNSON, E. L., WANG, C., JAFARI, A., YANG, C., SACKS, M. S., KRISHNAMURTHY, A. & HSU, M. 2021. Computational investigation of left ventricular hemodynamics following bioprosthetic aortic and mitral valve replacement. *Mech Res Commun,* 112.

YAMAURA, Y., ET AL. 2008. Three-Dimensional Echocardiographic Measurements of Distance Between Papillary Muscles and Mitral Annulus: Assessment With Three-Dimensional Quantification Software System. *J Echocardiogr,* 6**,** 67-73.

ZHANG, L. W., ADEMILOYE, A. S. & LIEW, K. M. 2019. Meshfree and Particle Methods in Biomechanics: Prospects and Challenges. *Archives of Computational Methods in Engineering,* 26**,** 1547-1576.